Active Flow Control Using Trailing-Edge Coanda Actuators in a Propeller-Driven Flow to Emulate Hover Flight

Thesis

Presented in Partial Fulfillment of the Requirements for the Degree Master of Science in the Graduate School of The Ohio State University

By

Victoria Aleksis Murnieks

Graduate Program in Aeronautical and Astronautical Engineering

The Ohio State University

2024

Thesis Committee

Dr. Jeffrey Bons, Advisor

Dr. Matthew McCrink, Committee Member

Abstract

Various trailing-edge (TE) Coanda active flow control (AFC) actuator configurations were experimentally investigated in a propeller slipstream flow to simulate hover flight. This thesis will provide a comprehensive evaluation of the configuration factors—in terms of spanwise position and geometric parameters—which impact the aerodynamic and control authority performance of TE Coanda AFC actuators in propeller-driven flow with no freestream velocity.

Two main types of TE Coanda AFC configuration experiments were conducted. The first type of testing involved varying the spanwise placement and size of TE AFC while maintaining constant internal geometry and circular Coanda profile shape with continuous slot blowing. The spanwise location testing's objectives were to determine the optimal Coanda AFC actuator location relative to the propeller slipstream and compare Coanda flow control effectiveness to that of a traditional deflection control surface. Two trailing-edge Coanda actuator sections of fixed spanwise length were designed, fabricated, and evaluated in terms of lift force and pitching moment generation at varying spanwise locations. Velocity profile measurements for this study for the case of no freestream flow indicated that the propeller slipstream is asymmetric over the NACA 0012 wing and contracts toward the side of the wing on which the propeller blade descends during rotation, where propeller downwash is experienced. This asymmetry

indicated that there may be an optimum location for Coanda AFC actuators at the wing trailing edge which couple with momentum from the propeller in regions of peak slipstream velocity.

The second type of testing involved varying TE AFC nozzle and surface profiles while maintaining constant spanwise location. These nozzles included both continuous and discrete slot blowing as well as sweeping jets. Surfaces investigated included circular, elliptical, and biconvex profiles. Each configuration was mounted to the trailing edge of a wing on a benchtop setup. A propeller at the leading edge provided a momentum source, and the lift and pitching moment were measured with a six-component load cell. The resulting load data was used to characterize the aerodynamic performance and control authority of each Coanda AFC configuration tested to determine which parameters—such as spanwise placement, Coanda AFC profile shape, slot size and spacing, and discrete vs. continuous slots—yield optimal performance for trailing-edge AFC. The efficiency of the actuators was evaluated using a modified form of momentum coefficient for the hover flight condition.

Dedication

To my parents, Kim and Raivo, who have always supported me, and to the many people who positively impacted my life here at Ohio State (especially my fiancé, Dylan).

Go Bucks!

Acknowledgments

I am grateful to have had so many supporters along my journey to complete this thesis focused on such a fascinating project. I thank my Research Advisor, Dr. Jeffrey Bons, as well as Dr. Matthew McCrink, for spearheading this Office of Naval Research (ONR) Vertical Takeoff and Landing (VTOL) project and getting me involved at the Ohio State Aerospace Research Center (ARC) while I was still completing my undergraduate degree. I also thank my coworkers on the ONR VTOL project, especially Dr. Alex Spens, Ross Heidersbach, and Anthony Pisano for their expertise, assistance, guidance, and encouragement.

Additionally, I am grateful to have a system of encouraging family and friends who have supported me through these past six years. I am especially grateful for my fiancé, Dylan Van Tassell, who constantly pushes me to be my best self and motivates me to accomplish major life goals, such as this.

Finally, I thank my colleagues at the ARC who welcomed me last year and have shared so much knowledge with me since—it has been a joy to work with you all!

Vita

2018……High School Diploma

Big Walnut High School

2021-2022……...Systems Engineering Intern,

Collins Aerospace

2023……B.S. Aerospace Engineering,

The Ohio State University

2023……Graduate Research Fellowship,

The Ohio State University

Publications

Murnieks, V. A., Spens, A., Heidersbach, R. W., Seth, D., McCrink, M. H., Bons, J. P., "Wing Trailing Edge Coanda Flow Control; Effect of Actuator Placement Relative to Upstream Propeller Slipstream," *AIAA SciTech 2024 Forum*, Orlando, FL, 2024.

Murnieks, V. A., Spens, A., Heidersbach, R. W., Seth, D., McCrink, M. H., Bons, J. P., "Effectiveness of Various Trailing Edge Coanda Actuator Nozzles and Surfaces with a Propeller Slipstream Flow," *AIAA SciTech 2024 Forum*, Orlando, FL, 2024.

Field of Study

Major Field: Aeronautical and Astronautical Engineering

Table of Contents

List of Tables

List of Figures

Nomenclature

A	=	Coanda surface semi-minor axis [m]
A_{AFC}	=	Active flow control injection nozzle area [m^2]
B	=	Coanda surface semi-major axis [m]
b	=	Wingspan [m]
b_{AFC}	=	Spanwise actuator length [m]
C_D	=	Drag coefficient
C_L	=	Lift coefficient
C_T	=	Propeller thrust coefficient
C_m	=	Pitching moment coefficient
$C\mu$	=	Momentum coefficient
c	=	Wing chord [m]
D	=	Propeller diameter [m]
dC_L/dC_μ	=	AFC lift gain
dC_m/dC_μ	=	AFC control gain
h	=	Coanda nozzle height [m]
J_{ss}	=	Slipstream momentum per actuator span [$kg/(m \cdot s^2)$]
L	=	Lift force [N]
M_z	=	Pitching moment [Nm]
$\dot{m}_{AFC}$	=	AFC mass flowrate [g/s]
R	=	Propeller radius [m]
r	=	Coanda actuator radius [m]

S = Wing planform area [m^2]

S_{AFC} = AFC reference area [m^2]

T = Propeller thrust [N]

TE = Trailing Edge

U_{AFC} = Exit slot velocity [m/s]

U_i = Propeller induced velocity [m/s]

U_j = Jet velocity [m/s]

U_{ss} = Propeller slipstream velocity [m/s]

U_∞ = Freestream velocity [m/s]

x = Horizontal chordwise distance [m]

y = Vertical spanwise distance [m]

z = Wing-normal distance [m]

Δ = Change in parameter

η = Radial distance from a curved surface [m]

θ = Coanda surface trailing edge angle

ρ_{amb} = Ambient density [kg/m^3]

ω = Propeller rotation rate [rev/min]

Chapter 1. Introduction

In modern military operations, the demand for versatile and agile aircraft capable of rapid deployment, precise maneuvering, and various mission profiles is critical. Vertical takeoff and landing (VTOL) aircraft have emerged as essential assets in military aviation since they can operate in confined spaces, navigate complex terrain, conduct covert operations, and respond expeditiously to evolving threats [1]. Furthermore, unmanned aerial vehicles (UAVs) can continuously fly longer missions than humans and reduce the dangers faced by humans during aircraft operation since pilots operate UAVs from remote ground locations as opposed to airborne cockpits. Combining the VTOL and UAV concepts in military aircraft increases the range and versatility of mission capabilities, as well as the safety of human operators [2]. Active flow control (AFC) is attractive for military vehicles due to its potential benefits of increased maneuverability and actuation response, as well as radar cross-section reduction for increased stealth. However, the optimization of AFC for VTOL UAV applications requires addressing challenges related to aerodynamic efficiency and control authority. This master's thesis focuses on the integration of Coanda actuator active flow control to VTOL UAVs with a focus on the performance of this technology in hover flight.

1.1 Background

This section explores the development of Coanda AFC effectors, first explaining the fundamentals of AFC and the mathematical parameters of focus for the scope of this thesis. This section will explain the Coanda effect, including how it has been used for AFC applications and its application to the VTOL UAV scenario in this work. Additionally, this section provides examples of aerospace engineering research that paved the way for the integration of Coanda technology in modern aircraft design. Finally, the gaps in existing research will be defined to identify the novelty of this research.

1.1.1 AFC Overview and Performance Parameters

Active flow control for aircraft control provides numerous benefits over traditional methods of movable control surfaces. Maneuverability can be increased by using flow control systems, as the movement of large, high inertia surfaces—traditional flap deflections—is not required. The weight and size of vehicles may also be decreased due to AFC integration by replacing large, heavy flap actuators with smaller valve systems. Because there is no need for deflecting control surfaces and their associated gaps, AFC-controlled aircraft may also produce the additional benefit of radar cross-section reduction, which improves stealth and is desirable for military flight vehicles. However, because pressurizing air incurs an efficiency penalty, AFC systems face the challenge of ensuring sufficient control authority and efficient use of pressurized air.

When assessing the performance of AFC, special attention is given to the implications of AFC actuation on lift force and pitching moment generation; these parameters represent aerodynamic performance and control authority, respectively. Lift is often presented in its nondimensional form, defined as the lift coefficient, C_L, presented in Eq. (1). In this equation, L represents the lift force, ρ_{amb} is the ambient density, U_∞ is freestream velocity, and S is the reference area of the lifting surface, which is equal to the full span (b) multiplied by the full wing chord (c) in this traditional definition.

$$C_L = \frac{L}{\frac{1}{2}\rho_{amb}(U_\infty)^2 S} \tag{1}$$

Similarly, pitching moment is represented in its nondimensional form as the pitching moment coefficient, C_m, presented in Eq. (2). In this equation, M_z is dimensional pitching moment, and all other variables are the same as defined for Eq. (1) with the addition of the wing chord, c, in the denominator to ensure the dimensions of the numerator and denominator cancel. Note that this equation is used for examining lift over a wing from its leading edge when a moment is applied at the trailing edge, so the entire wing chord is used for normalization.

$$C_m = \frac{M_z}{\frac{1}{2}\rho_{amb}(U_\infty)^2 c * S} \quad (2)$$

Eq. (1) and (2) are the conventional lift and pitching moment coefficients [3]. These equations will be modified from their conventional forms—for application to the hover flight case using an alternate velocity for reference—in this work.

Another parameter specific to defining active flow control performance is the momentum coefficient, $C\mu$, which is presented in Eq. (3). The momentum coefficient is a metric representing the momentum flux of the AFC component over the dynamic pressure (or momentum flux) of the freestream component of an AFC system [4], [5]. Momentum coefficient is often viewed as a cost metric since it measured the momentum flux of AFC blowing vs. freestream blowing supplied to AFC.

$$C_\mu = \frac{\dot{m}_{AFC} U_{AFC}}{\frac{1}{2}\rho_{amb}(U_\infty)^2 S} \quad (3)$$

In Equation (3), $\dot{m}_{AFC}$ is the mass flow supplied to an AFC source, U_{AFC} is the AFC velocity, and the denominator variables are the same as defined for Eq. (1) and Eq. (2). This performance parameter will also be modified from its conventional form to be applicable for the hover flight case where freestream flow is not present.

1.1.2 The Coanda Effect

The Coanda effect is a phenomenon where a fluid adheres to a curved surface, which will be fundamentally elaborated on in the following chapter. This effect presents a compelling opportunity for active flow control in VTOL aircraft. By strategically manipulating airflow over control surfaces through Coanda actuation, these aircraft can achieve improved lift and controllability [4], [6], [7]. Integrating Coanda actuators can elevate the performance of military VTOL platforms, offering advantages in both hover and forward flight modes. Incorporating trailing-edge (TE) AFC actuators in hover flight is the focus of studies that comprise this thesis. Figure 1 displays a TE Coanda AFC schematic. In this schematic, solid black lines depict surfaces of the Coanda actuator, and the left side is merged with the wing such that AFC is sourced from an internal plenum. Note that this schematic intends to represent a full circular Coanda surface; the dashed line at the bottom represents a line of symmetry for a symmetric airfoil.

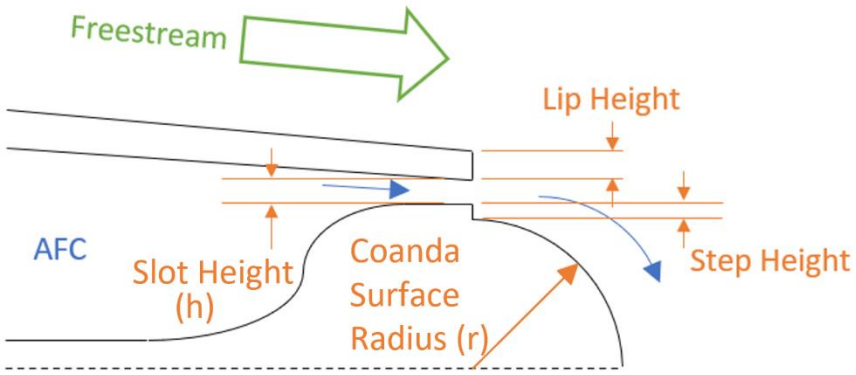

Figure 1: Schematic of TE Coanda AFC system.

The origin of Coanda actuation can be traced back to Henri Coanda, scientist from Romania who conducted a multitude of experiments on fluid dynamics and flight tests in the early-to-mid 20th century, identifying the aforementioned ‘Coanda effect’ in 1932 [8]. Henri Coanda initially understood the Coanda effect as the tendency of fluid to follow a curved surface due to a ‘vacuum’ created between the fluid and surface and applied this concept into many of his subsequent designs [9].

Present-day researchers now understand the Coanda effect in more detail as being a result of the radial pressure gradient that occurs within a fluid as it encounters a curved surface. This pressure gradient is caused by the wall curvature, with lower pressure closer to the convex wall. In other words, when a jet of fluid encounters a curved surface, the fluid experiences a radial (cross-stream) pressure gradient and adheres to the surface due to the ambient pressure being greater than that of the fluid jet near the wall; the atmosphere effectively presses the fluid against the curved surface. Equation (4) mathematically describes the tendency of a jet of fluid to remain attached to a curved surface due to the balance between the pressure and centripetal acceleration [10]. The balance between the left-hand side—radial pressure gradient—and the right-hand side—centripetal acceleration—of this equation enables the Coanda effect; without this force balance, flow attachment will not occur.

$$\frac{dP}{d\eta} = \frac{\rho U_j^2}{r + \eta} \tag{4}$$

In Eq. (4), dP is the pressure change in the radial direction across the jet of fluid, η is the radial distance from the curved surface, ρ is the ambient density, U_j is the jet velocity, and r is the Coanda surface radius. Figure 2 displays the variables from Eq. (4) in this context with the solid black lines depicting surfaces.

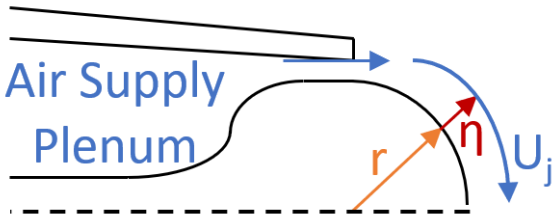

Figure 2: Depiction of Eq. (4) variables, adapted from Wilde [10].

1.1.4 Sweeping Jet AFC

Fluidic oscillators (FOs) are devices which use the Coanda effect to manipulate air flow through internal fluidic feedback systems and generate jets which sweep back and forth in the spanwise direction, as shown in Figure 3. A FO generates a sweeping jet at its exit purely through the recirculation of incoming flow as it adheres to the internal curved surfaces with no moving parts required. Srinivas et al. reported in their 1988 study

of FOs that these devices are attractive to the aerospace community due to their provided benefits of self-excited oscillating and enhanced mixing of exit flow with ambient fluid [11]. However, this study also reported notable drawbacks of their FOs which included pressure buildup in the central plenum and no improvement in flow mixing over steady jets [11].

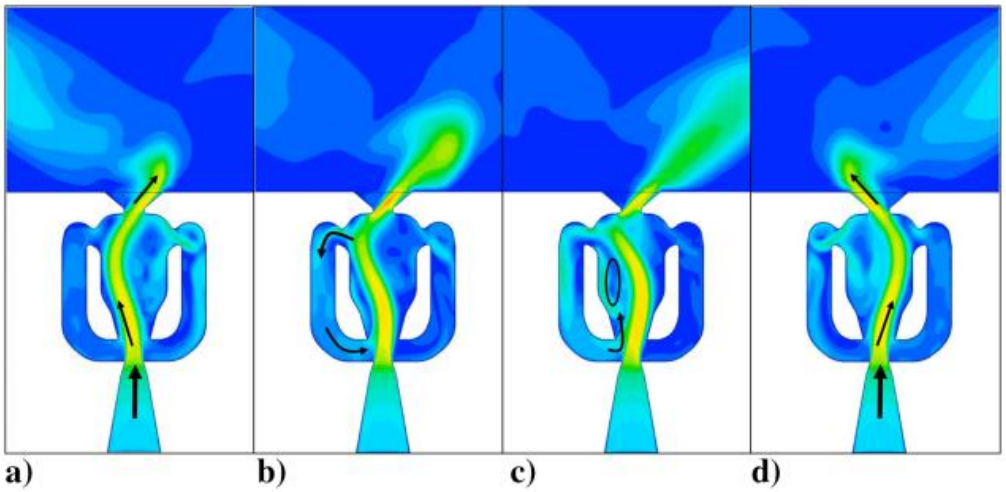

Figure 3: Pressure contour representation of a FO flow switching cycle [12].

More recently in the 21st century, more work has been done to optimize the shape and performance of FOs. Woszidlo and Wygnanski studied the effects of spanwise FO arrays when incorporated into varying airfoil deflection sizes and angles [13]. DeSalvo et al. conducted similar studies focusing on the effect of one spanwise FO array onto a flap with varying deflection angles [7]. Both studies found lift improvements with the use of FO arrays combined with a deflected surface compared to a traditional deflected surface

with no FO actuation. This was due to improved flow attachment along the airfoil surface due to freestream flow mixing with FO exit flow which generates streamwise vortices. These streamwise vortices alternate in time as the flow switches attachment sides due to recirculation through the feedback channels. This switching—also known as oscillation—between sides of the FO exit slot produces a sweeping jet that disperses exit airflow over a greater axial range than that of the exit slot from the continual back-and-forth motion at the exit. In a similar report, Koklu compared the performance of FOs with other flow control methods for maintaining flow attachment over a curved ramp surface [14]. This study found that FOs outperformed the AFC methods of vortex generating jets (VGJs) and discrete jets by maintaining attached flow due to increased chordwise coverage of exit flow, as well as increased mixing with the freestream flow source [14].

Most related to this thesis, Vukasinovik et al. compared FO jet performance to continuous slot jet performance on an airfoil with flow exiting over a half-circular Coanda profile and found that an array of FOs produced near equal lift values, ΔC_L, to continuous slot actuators at the same blowing coefficient, $C\mu$ [15]. This study also found that the airfoil with an array of FOs exiting onto the Coanda surface experienced consistently lower drag values, ΔC_D, at the same $C\mu$ [15]. These results are promising in that they indicate FOs can produce the same aerodynamic benefit as continuous slot Coanda actuators with less penalty. The component of the present work in which AFC geometric configuration is varied aims to form a similar comparison between FO array and continuous slot performance over a Coanda surface, as well as varying other Coanda

surface and jet parameters. The present body of work aims to build upon this information by evaluating the performance of FOs over a fully circular Coanda surface.

1.1.5 Relevant Flight Vehicles

A review of literature related to VTOL UAVs and in aerospace engineering reveals numerous experimental vehicles for varying applications throughout the past eight decades. Starting in the 1950s, the United States Navy began constructing and testing experimental tail-sitter VTOL vehicles for intended use on aircraft carriers for rapid and versatile deployment of airpower [16]. The concept of applying this technology was attractive but researchers developing early VTOL tail-sitters—such as the XFY-1 and the XFV-1 (scale model pictured in Figure 4)—faced challenges related to stability and control, especially during takeoff and landing [17]. These challenges were due to the manned and UAV tail-sitter designs being top-heavy, causing unreliable landing performance, leading to a stagnation in plans for VTOL tail-sitter production. Although VTOL tail-sitters were deemed an impractical design for full-scale manned and UAV mission use, research of these technologies continued through into the 1960s before Congress re-allocated funding to short takeoff and landing (STOL) aircraft development [18], [19].

Figure 4: Photograph of a 25% scale model of the XFV-1 aircraft [20].

With the emergence of more reliable and controllable UAV technology in the 21st century, the United States Navy has a reinvigorated drive for bringing VTOL UAV technology to full maturation. The Office of Naval Research (ONR) has several ongoing projects and efforts focused on developing VTOL UAV technology, one being the basis for the research presented in this thesis. The present study's purpose is to inform a project which will integrate AFC into a tail-sitting VTOL UAV to be used as the primary vehicle control source. This thesis analyzes design decision factors which impact performance of

Coanda AFC effectors on the trailing-edge of a wing—to replace traditional flap deflections—in hover flight.

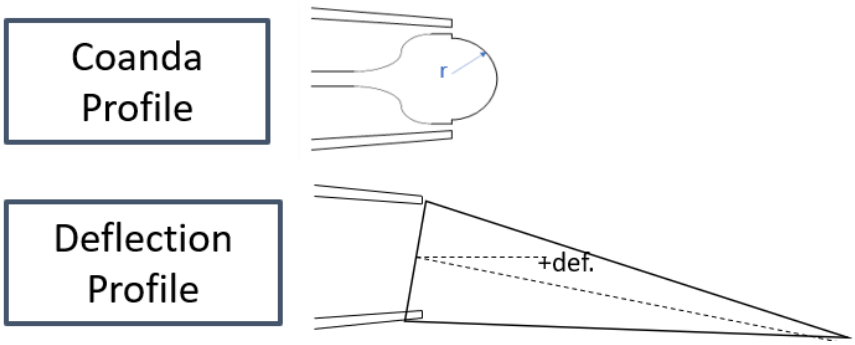

Figure 5: Schematic comparing Coanda surface to traditional deflection profile.

The conception of flight vehicles which intentionally harness the Coanda effect using AFC can be traced back to the 1930s with Henri Coanda's flight testing research. One of Coanda's designs which is particularly relevant to this thesis was a disk-shaped VTOL aircraft named the 'flying saucer' [8]. This vehicle was more recently replicated in the 1970s by the United States Air Force in a vehicle called the Avro VZ-9V, which was not further developed due to engine complications and lack of both pressure and flow rate supplies to achieve stable hover [9]. Although the flying saucer design of this vehicle may seem like an effort focused solely on bringing science fiction into the real world, it is a notable example of how the Coanda effect can be harnessed for hover flight through

AFC which is extremely relevant to this work. Figure 6 displays a side-view drawing and top-view photo of the AVRO VZ V9.

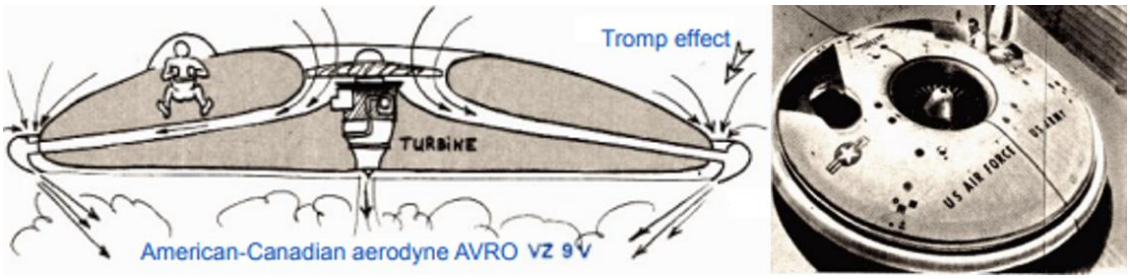

Figure 6: AVRO VZ 9V "flying saucer" vehicle [9].

More recent research in the 21st century has been conducted for AFC for flight vehicles to demonstrate that this technology has viability and applications greater than science fiction thought experiments. Two examples of STOL vehicles which operate through fluidic control systems rather than traditional flap deflections are the DEMON and MAGMA flight vehicle demonstrators [21], [22]. These vehicles were created in 2010 and 2017, respectively and use bleed air from their main propulsion sources to power their AFC systems [6]. Figure 7 displays the planform drawings and photos of these vehicles; special attention should be paid to the trailing edges of these drawings where Coanda AFC effectors were located. These vehicles are particularly relevant to this thesis due to their in-flight demonstration of Coanda AFC for trailing-edge pitch control, proving the viability of this technology integration and application.

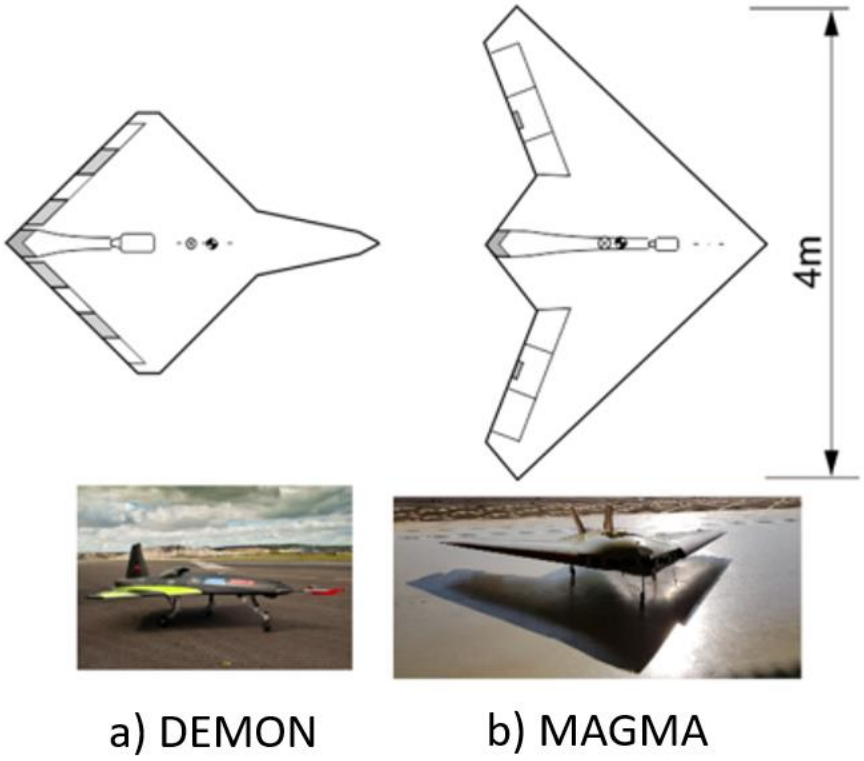

Figure 7: Depictions of the DEMON and MAGMA demonstrator vehicles [6].

One example of ongoing flight vehicle research aimed at harnessing AFC for primary control is occurring at the Illinois Institute of Technology (IIT) under the group led by Dr. David Williams [23]. The IIT group has developed a flight vehicle which uses Coanda effectors for control, much like the present work aims to do, with the main project difference between being that the IIT aircraft is of STOL configuration rather than VTOL [24]. Despite this difference, the research and flight testing conducted by IIT is promising in that they have proven that Coanda effectors can replace flap deflections for effective control. One key technology which enabled the IIT group's success was the capability for switching the Coanda surface to direct flow in multiple directions, as shown from the side

in Figure 8 with tufts wrapping in the direction of blowing [25]. Although the present work examines unidirectional Coanda flow control, the adoption of multidirectional Control will be necessary for maturation of this project to the flight vehicle stage.

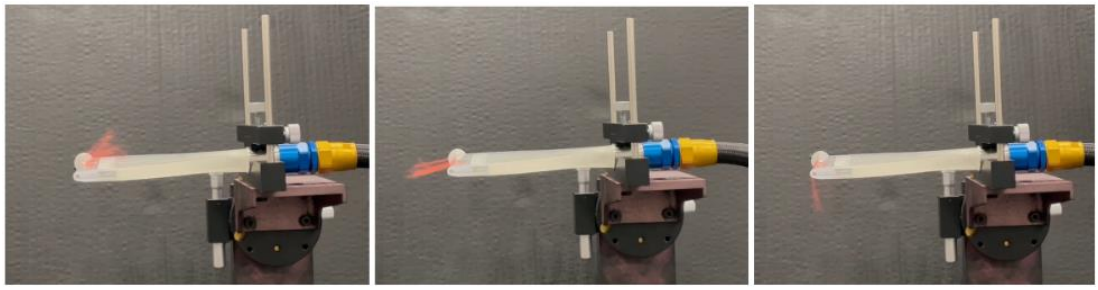

Figure 8: Multi-directional Coanda AFC actuator developed by IIT [25].

Another notable ongoing AFC research endeavor is the CRANE (Control of Revolutionary Aircraft with Novel Effectors) project which the Defense Advanced Research Projects Agency (DARPA) is undertaking [26]. The DARPA CRANE project aims to accomplish a similar goal to the present body of work by replacing conventional control deflections with AFC, the main difference being that the CRANE vehicle is a STOL configuration rather than VTOL and aims to harness multiple AFC technologies in addition to Coanda surfaces control effectors [27], [28]. Like the DEMON and MAGMA demonstrator vehicles, the CRANE vehicle aims to harness Coanda AFC effectors to replace traditional trailing-edge control surfaces and use distributed bleed air from the primary propulsion source to provide mass flow to the AFC system.

1.1.6 Identifying the Research Gap

Section 1.1.5 Relevant Flight Vehicles demonstrated that vehicles have been designed, built, and flown to demonstrate capabilities of tail-sitting VTOL UAV technology and control authority through AFC. However, these emerging technologies have never been combined into a single flight vehicle; a tail-sitting VTOL UAV has not yet been designed with AFC as the primary control source, and that is where the information from this thesis will be used. Furthermore, the effect of TE Coanda AFC effectors have not yet been studied on a wing with propeller-driven flow and no freestream momentum source, which makes the work presented in this thesis especially unique as this propeller-wing combination can inform the aerospace community on the performance of AFC in hover flight. Finally, this thesis intends to bridge information across studies by comparing the performance of different Coanda AFC configuration parameters to include the profile shape as well as the nozzle type—sweeping jets, discrete jets, and continuous slot.

1.2 Thesis Objectives

This thesis seeks to investigate the impact of TE Coanda AFC on aerodynamic performance and control authority of VTOL aircraft, with a specific focus on hover flight. Through two primary experimental investigations, this research aims to understand the capabilities and limitations of TE Coanda AFC actuators. The first investigation characterizes the effect of TE Coanda AFC spanwise location in relation to the slipstream

of an upstream propeller. This spanwise location investigation first characterizes how propeller slipstream is affected by propeller-wing interactions then establishes a relation between control authority to local momentum flux experienced by the TE Coanda AFC actuator. The second investigation characterizes the effect of altering various Coanda actuator surface and nozzle characteristics to determine which geometric parameters optimize aerodynamic lift and pitching moment control performance.

1.3 Thesis Layout

The next chapter of this thesis will describe the procedures and test conditions for experiments conducted and the data analysis methods used for processing results. Following this, the results chapter will present and discuss the outcomes from experiments and analysis. Finally, the conclusion chapter will present overall impacts of and key takeaways from the work presented in this thesis.

Chapter 2. Experimental Setup and Methods

This chapter will describe the experiments conducted with Coanda AFC effectors, which includes two main experiment types: (1) varying spanwise AFC location and (2) varying geometric configuration of AFC. The experimental setup will first be explained, with detailed descriptions of the setup, equipment, and test conditions for each type of experiment. Next, the methods used for data analysis and processing will be described.

2.1 Experimental Setup

To analyze the influence of spanwise actuator position on the resultant forces and moments experienced by the wing, a tabletop static setup was developed with capability to reconfigure the trailing edge with AFC actuators and traditional deflected control surfaces. To map the propeller slipstream over the wing, velocity profile data were collected using a Kiel probe configured perpendicular to the wing's surface which traversed along the chordwise and spanwise directions of the wing while maintaining equal offset distance of 10mm from the surface. Following the velocity profile analysis, the testing was conducted to vary the spanwise location of AFC actuators along the trailing edge to identify the optimal spanwise location in terms of lift force and pitching moment generation by AFC at each location and compare the effect of AFC to a traditional deflection surface.

After the varying spanwise AFC location tests, various Coanda actuator systems were experimentally evaluated for their effectiveness and costs. Both the nozzle type (continuous slot, discrete, or sweeping jet), and Coanda surface were varied. The same benchtop setup as the varying spanwise location tests—consisting of a propeller, wing, and trailing edge actuator—was used with varied trailing-edge attachments for each AFC configuration to evaluate the effectiveness of each.

2.1.1 Static Test Stand Configuration

Figure 9 displays the static test stand with its trailing edge configured for AFC testing at the center-span location. The wing in this setup was a NACA 0012 symmetric airfoil with geometry parameterized by the propeller radius R=0.19m. This wing had a chord length of 0.392m (c = 2.06R) and a wingspan of 0.614m (b = 3.22R). This wing was composed of a foam core internal structure encased in a fiberglass shell.

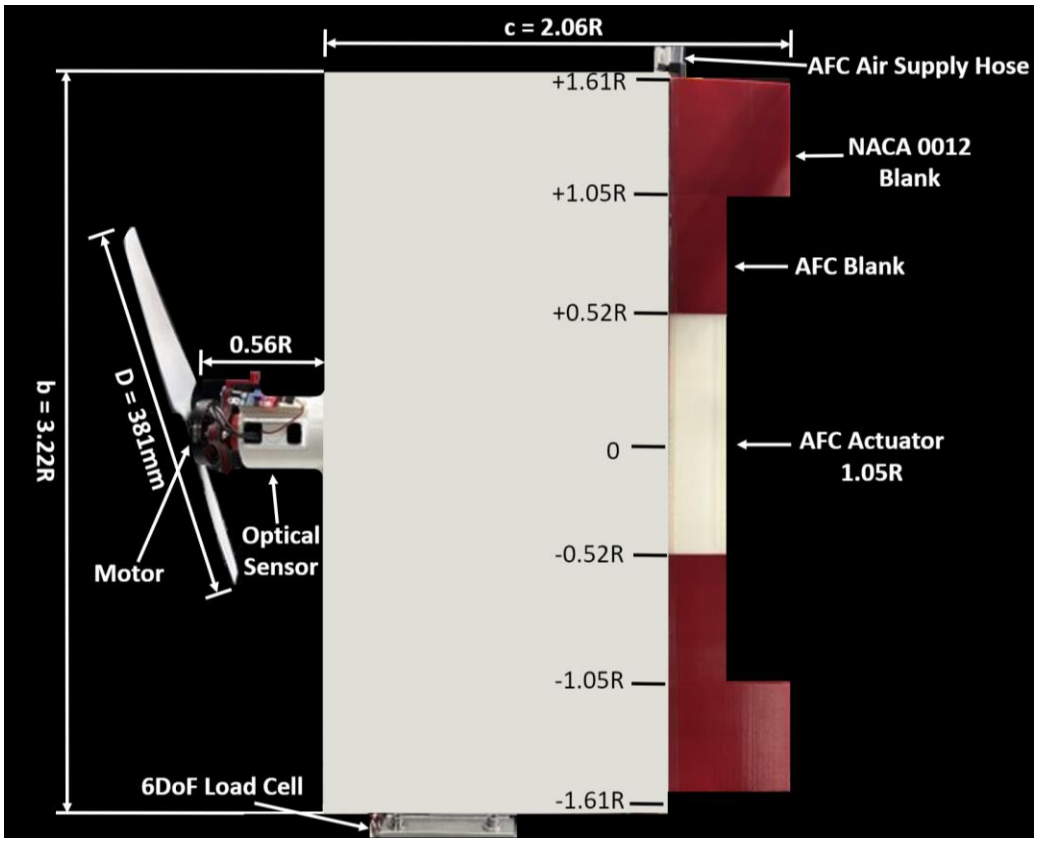

Figure 9: Propeller-wing setup with 200mm AFC at center-span and 0° trailing edge deflection of blank sections.

At the trailing edge, a custom "zipper" attachment—CAD design displayed in Figure 10 and interface displayed in the left image of Figure 11—was 3D printed and integrated into the wing's structure at the 75% chord location. The part on the top left was merged with different trailing edge configurations—AFC actuators, blank sections, and traditional deflected control surfaces. The part on the bottom left was inserted directly into the wing in the spanwise direction, where it remained; on the right, the interface between these two parts is shown. This zipper allowed for different trailing edge configurations to be easily interchanged to test various conventional control surfaces and AFC control actuators.

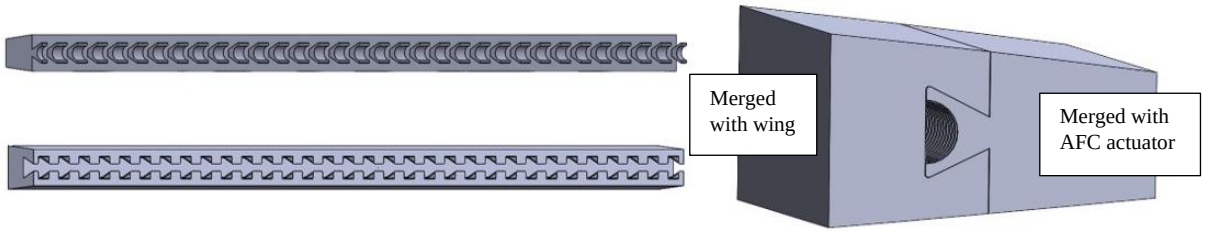

Figure 10: Zipper attachment interface at trailing edge of wing.

In addition to evaluating the effectiveness of TE Coanda AFC actuators, traditional deflected surfaces were tested on this static test stand setup. The traditional deflection surfaces were designed with the same NACA 0012 profile as the wing with which they were interfaced using the zipper trailing edge attachment. The zipper interface attachment pieces used to lock the deflected surface are shown in the bottom right of Figure 11, along with a top view example of the deflection—spaced with the 30° control lock piece attached to the trailing edge—in the top right image. Note that tape was placed and smoothed over the interface between the TE effectors and the wing during experimentation for AFC and traditional deflection configurations. The type of tape used was Scotch® Tape 600, with chordwise thickness of 0.025m (0.065*c*) and total *z*-axis thickness of 5.8×10^{-5} m perpendicular to the wing's surface on each side [29]. This was done to eliminate any gaps which could disrupt the flow field and alter results.

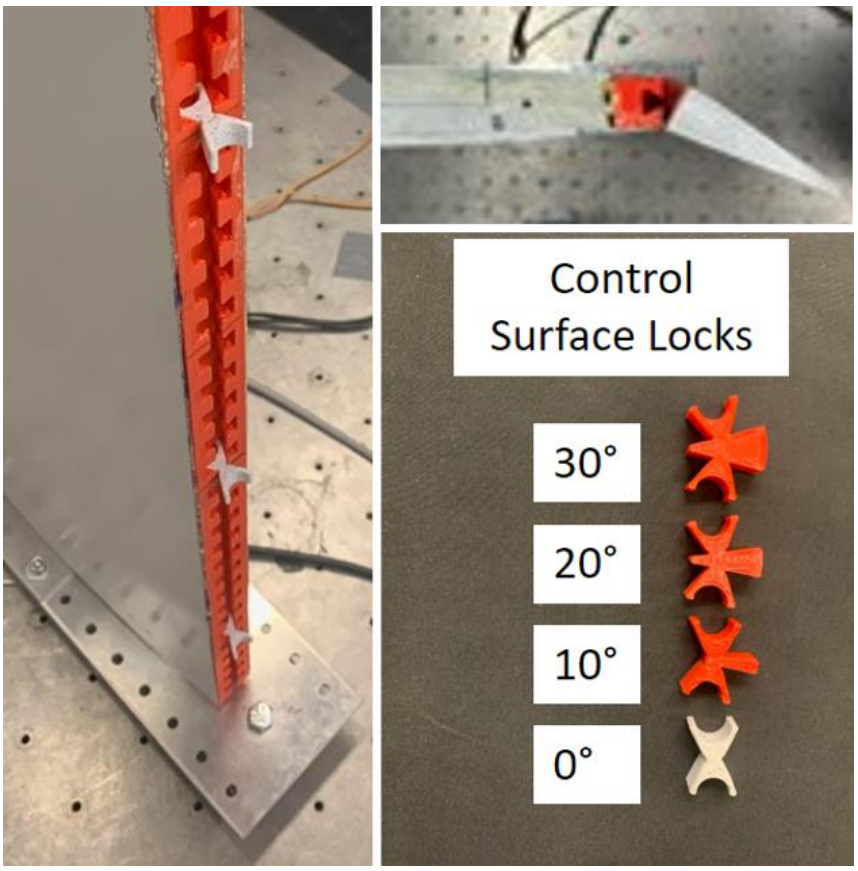

Figure 11: Zipper interface embedded in wing with top view of control surface locks and NACA 0012 profile deflection attachment [30].

In section 1.1.5 Relevant Flight Vehicles, Figure 5 displays a schematic of the traditional deflection compared to the Coanda surface profile. The Coanda actuator operates with one-sided blowing for the experiments in this work, blowing air from only the top slot in the Figure 5 schematic. Note that the traditional deflection spanned 200mm of the trailing edge, not the entire 614mm wingspan—and was fixed at the center-span location during testing to provide a direct comparison with the 200mm Coanda AFC actuator. To further ensure direct comparison between testing, the same blank geometry

configuration shown in Figure 9 was used when testing the traditional deflected piece at center-span.

The leading-edge cowling was used to mount an RPR-220 optical sensor to measure the rotational rate of the propeller during operation. A T-Motor Antigravity MN-5006 motor was used to power a 0.381m diameter by 0.142m pitch (15-in diameter by 5.6-in pitch) propeller located 0.107m from the wing leading edge. The propeller standoff distance was 0.56 times the radius ($x_{LE} = 0.56R$) and the distance from the propeller to the trailing edge was 2.62 times the radius ($x_{TE} = 2.62R$). All wiring for the motor and optical sensor was routed internally within the cowling and wing structure to minimize protruding surfaces which could impact the flow physics. Motor control was provided by an electronic speed controller (ESC) regulated with a Proportional Integral Derivative (PID) control system implemented through an Arduino microcontroller. The wing was connected to the table via an ATI Gamma six-degrees-of-freedom (6 DoF) load cell, which was used to measure the resultant forces and moments at the quarter-chord location ($x_{LC} = 1.08R$). All data were gathered using Data Acquisition Systems (DAQs) controlled through a custom LabView program. With this instrumentation setup, the measurement uncertainties of data collected were 1.2% and 2.5% for lift force and pitching moment, respectively. These uncertainties were computed by dividing the load axis resolution values from the ATI Gamma online datasheet by the minimum change in values of data acquired during testing [31]. The measurement uncertainty for pressure was 2.5%, which was computed as the maximum standard error of the measured signals and thus can be applied to each measured value.

Table 1: ATI Gamma sensor ranges and resolutions for load axes [31].

	Fx, Fy	Fz	Tx, Ty	Tz
Sensing Range	0-32 N	100 N	0-2.5 Nm	0-2.5 Nm
Resolution	0.00625 N	1.25 N	0.0005 Nm	0.0005 Nm

2.1.2 Coanda AFC Design and Characterization

The next two subsections will describe the design and manufacturing process for the TE Coanda AFC actuators in the experiments which evaluated the effect of varying AFC spanwise location (section 3.1.2.1) and varying AFC geometric configuration (section 3.1.2.2). Also, specifications such as the exit slot velocity distribution and sizing of each AFC actuator are in the following two subsections.

2.1.2.1 Varying Spanwise AFC Location Characterization

The Coanda AFC actuator design used in the varying spanwise location experiments was a continuous slot with a spanwise dimension of 0.2m=200mm (1.05R) and a circular surface profile which was 3D printed with PLA filament. A sectional model of the trailing edge Coanda actuators is shown in Figure 12, which displays a side view of the actuator in the orientation it was mounted to the wing (with AFC feed line from above), as well a top view of the Coanda surface profile with key dimensions. This Coanda actuator was designed and fabricated with a radius of r=8mm, slot height of h=0.5mm, and lip height of 0.7mm. Note that the step height—a parameter defined and

depicted in Figure 1—for this Coanda actuator was 0mm. This figure also displays arrows indicating the path of airflow through the actuator in the top and side views.

Air was expelled from only one side of the chord line to ensure the Coanda actuators provided load effects comparable to traditional control surfaces. Furthermore, to ensure symmetry of geometry and balance of forces when AFC was implemented on the trailing edge, there was a symmetric ‘blank’ geometry on the opposing side of the wing which mirrored the external geometry of the blowing side but was sealed off with a solid wall to prevent airflow. AFC actuators were oriented to wrap the flow from slot blowing around the trailing edge and produce moment in the same direction as the traditional deflections, effectively yielding a trailing-edge-down moment and lift force.

Along the remainder of the wing in locations without Coanda actuators, blank trailing edge pieces were installed. There were two varieties of blanks (Figure 9). The first followed the original profile of the NACA 0012 airfoil and was used at the wing tips. The second had the same profile as that of the Coanda actuators with the exception that both sides of the chord line featured the sealed-off geometry explained in the previous paragraph. Both blank designs had a hollow section to allow for the passage of the air supply tube feeding the AFC.

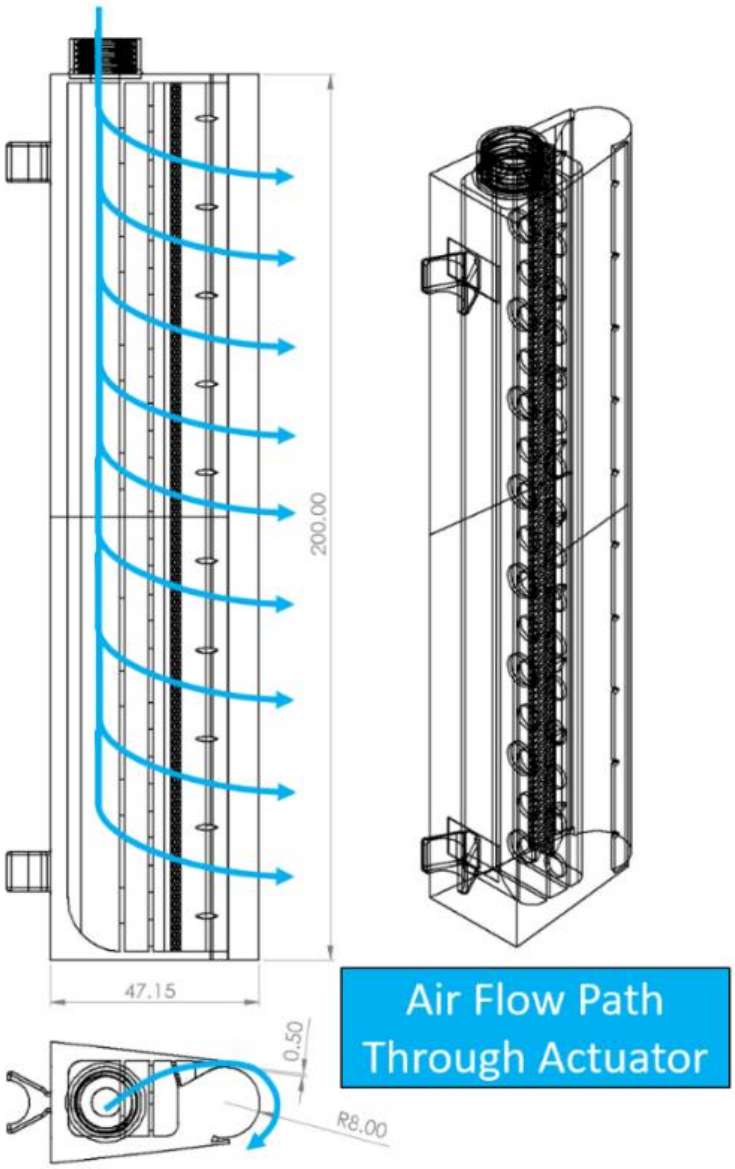

Figure 12: Baseline design of trailing-edge Coanda actuator (ID CC-R8-H0.5).

The controlled air was connected to the wing and trailing edge actuators by a flexible hose, which was positioned and secured above the wing to minimally impact load cell readings. This hose then routed internally through hollow non-AFC trailing-edge

sections to supply air directly to the Coanda actuator. Finally, the air passed through the actuator's three internal diffusion grids to provide a uniform flow distribution at the exit slot for continuous slot-blowing. To evaluate spanwise exit slot blowing uniformity, a pitot-static probe designed for boundary layer measurements was positioned with its hooked end 0.5mm inside the AFC exit slot recess—between the top and bottom lip of the exit slot. The boundary layer probe traversed nine 20mm increments to collect spanwise velocity measurements at the exit slot. This traverse testing was repeated five times for the 200mm actuator and concluded that the variation was less than 9% from the average value along the span. Figure 13 and Table 2 display the exit slot velocity distribution of this 200mm AFC actuator.

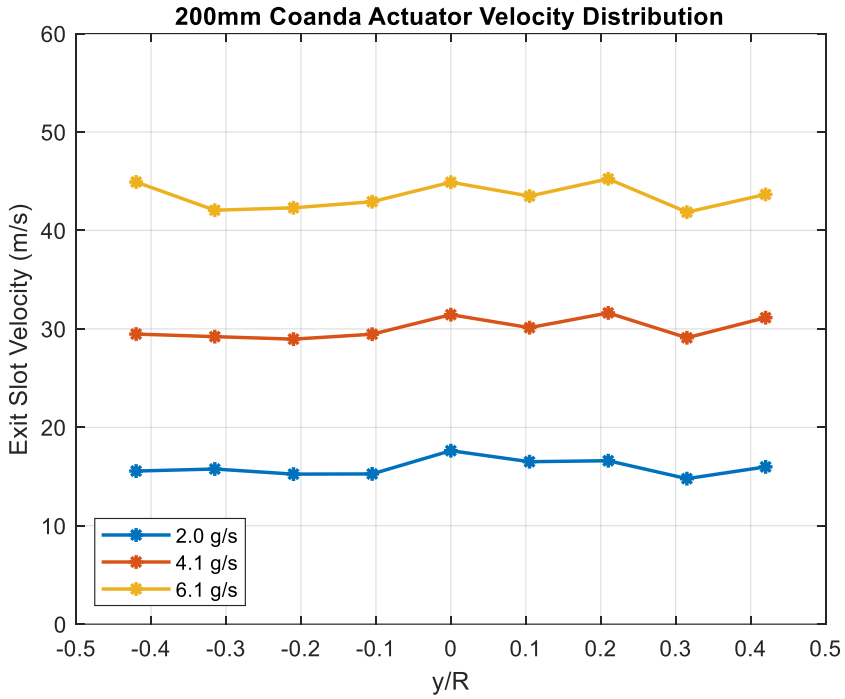

Figure 13: Velocity distribution of 200mm Coanda actuator in varying spanwise location tests, conducted inside the AFC exit slot recess with a boundary layer probe.

Table 2: Exit slot velocity characteristics of 100mm Coanda actuator in varying spanwise location tests.

Mass Flow (g/s)	Average Velocity (m/s)	Minimum Velocity (m/s)	Maximum Velocity (m/s)	Percent Variation (%)	Standard Deviation (m/s)
2.0	15.92	14.78	17.63	17.85	0.82
4.1	30.06	28.96	31.62	8.86	1.01
6.1	43.48	41.86	45.24	7.78	1.23

A 0.1m=100mm (0.52*R*) Coanda actuator was designed with the same internal geometry and external profile as the original 200mm actuator, only half the span. This

half-span actuator was fabricated on the same 3D printer with the same settings and material as the original 200mm actuator to ensure the surface finish and manufacturing were equal. An additional 100mm of trailing-edge blank sections matching the circular Coanda profile were introduced when testing this 100mm actuator to ensure the wing aspect ratio remained the same between the 100mm and 200mm AFC tests. Note that this substitution of AFC section for blank sections changed the measure of TE span which was consumed by non-Coanda geometry which could lead to inherent differences in the data acquired between the two configurations on the same test stand. The purpose of developing this shorter-span actuator was to achieve a more refined analysis of the effect of trailing-edge Coanda actuator placement by using an actuator spanning approximately half of the upstream propeller radius as opposed to the original Coanda actuator which spanned 52% of the propeller radius. Exit slot uniformity evaluation for the 100mm actuator was conducted using the same procedure as for the 200mm actuator, with one difference being that traversing was conducted in 10mm spanwise increments for this shorter-span actuator. This uniformity data demonstrated that the exit slot velocity across the 100mm span was within 7% variation from the average value for all mass flow rates tested. Figure 14 and Table 3 display the exit slot velocity distribution of this 100mm AFC actuator.

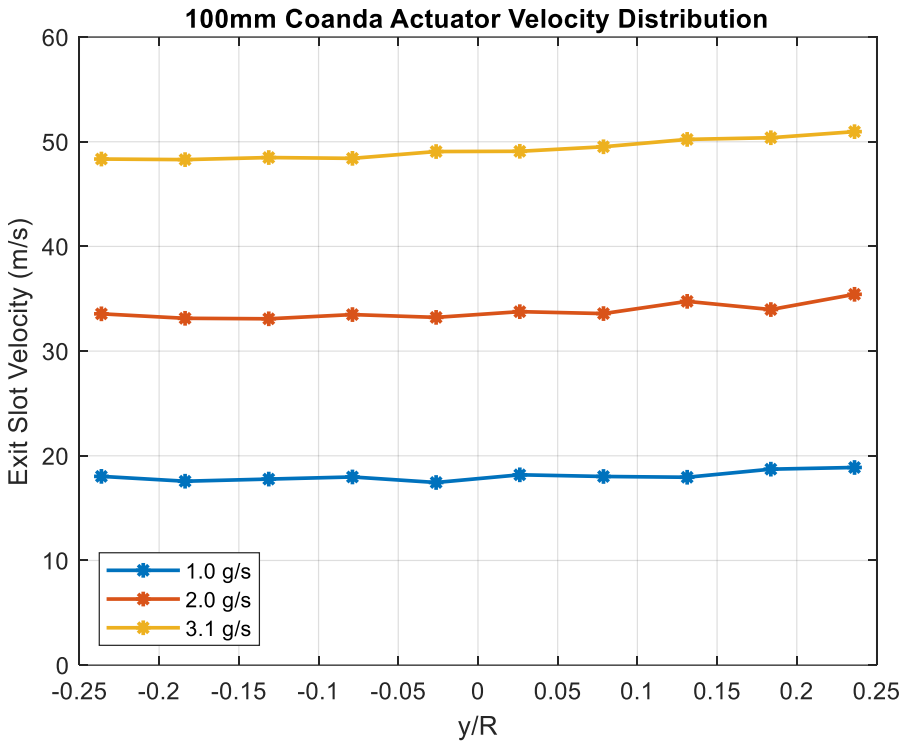

Figure 14: Exit slot velocity distribution of 100mm Coanda actuator in varying spanwise location tests, conducted inside the AFC exit slot recess with a boundary layer probe.

Table 3: Exit slot velocity characteristics of 100mm Coanda actuator in varying spanwise location tests.

Mass Flow (g/s)	Average Velocity (m/s)	Minimum Velocity (m/s)	Maximum Velocity (m/s)	Percent Variation (%)	Standard Deviation (m/s)
1.0	17.45	18.88	18.06	7.93	0.43
2.1	33.09	35.43	33.80	6.92	0.71
3.1	48.29	50.96	49.28	5.42	0.91

2.1.2.2 Varying AFC Geometry Characterization

A subset of nozzle types and surfaces was selected based on previous successful results in published literature. Seven continuous slot Coanda actuators and seven discrete slot actuators (including sweeping jets) were fabricated with 3D printing methods using PLA filament. These 14 actuators were first evaluated for their exit slot uniformity performance. Three nozzle types were examined: a continuous slot, an array of spanwise discrete jet slots, and an array of spanwise fluidic oscillator sweeping jets (Figure 15). Similarly, three Coanda surface profile shapes were examined: circular, elliptical, and biconvex (Figure 16). A variant of the circular shape was introduced as a half-profile.

The elliptical profile designs were inspired by work from Alexander et al. who studied elliptical Coanda profiles and found that longer elliptical Coanda surfaces in the *x*-axis improved flow attachment to the surface [32]. Building upon this idea, the bi-convex Coanda surfaces were designed to evaluate a surface shape that was both rounded and tapered to improve surface flow attachment. This study aimed to compare elliptical and bi-convex Coanda performance with the more conventional circular shape. If these aerodynamically shaped surfaces were to yield comparable lift and pitching moment performance to circular Coanda surfaces, substitution could be made to implement an elliptical or bi-convex Coanda surface design for reduced drag, which is a hindrance to circular Coanda surface designs [22].

Typically for full pitch control, a set of nozzles on both sides of the chord line is required. However, due to the unique flow field created by wing-propeller wake interactions two adjacent half circular actuators oriented with slot blowing in opposite

directions and aligned with regions of maximum trailing edge velocity profile may be more effective for pitch control. The study by Johnson et al. demonstrated that the propeller slipstream velocity for the hover condition skews toward the side of the wing which experiences the upstream propeller's descending blade [33]. This causes the trailing-edge velocity to be greatest in a spanwise location biased toward the descending blade rather than the center span location due to asymmetric vortex contraction. Other parameters were also varied such as nozzle spacing and trailing edge radius. A trailing edge Coanda actuator with circular profile, radius r=8mm, and slot height h=0.5mm (ID CC-R8-H0.5) was the baseline design.

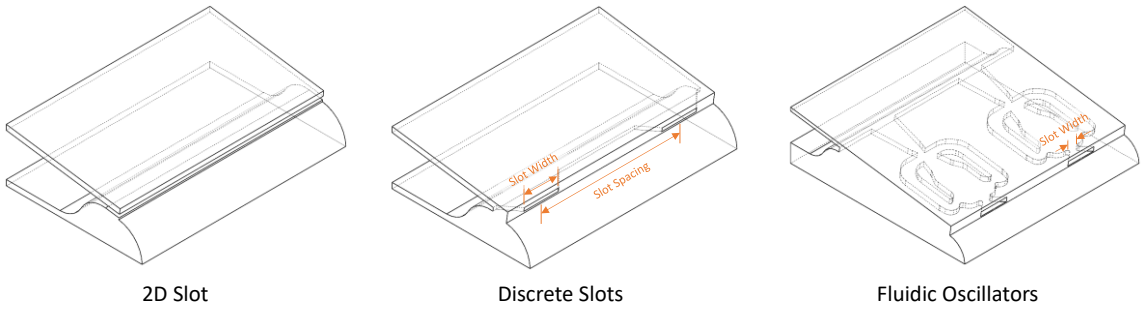

Figure 15: Coanda AFC actuator nozzle internal geometries.

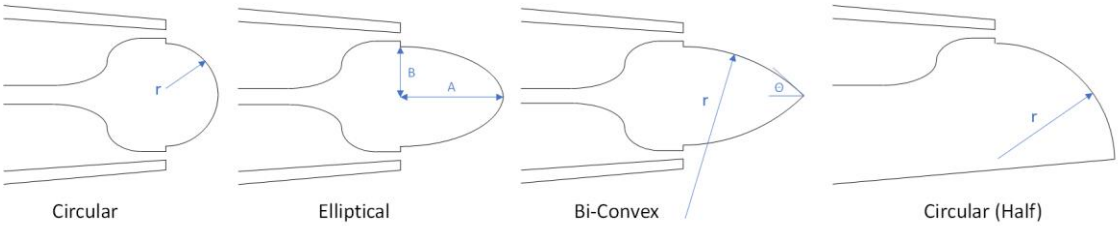

Figure 16: Coanda AFC actuator surface profile geometries.

For continuous actuator IDs in Table 4, the first character “C” signifies that the design has a continuous slot. The second character represents the Coanda profile shape: “C” for circular, “E” for elliptical, and “B” for bi-convex. The second set of characters for circular and bi-convex designs begins with “R” followed by the radius measurement in mm. All bi-convex actuators were designed with an angle between the Coanda surface and trailing edge of θ=45 degrees. For elliptical designs, the second set of characters begins with “A” followed by the semi-major axis measurement in mm, and the third set of characters begins with “B” followed by the semi-minor axis measurement in mm. For all continuous designs, the final set of characters begins with “H” followed by the slot height measurement in mm. Varying external geometry while also maintaining the NACA 0012 profile caused the moment arm to change for each continuous slot actuator tested. This moment arm variation was accounted for in moment analysis and values are detailed in Table 4.

Table 4: Characteristics of continuous slot actuators with varying profiles.

Actuator ID	*h/r* or *h/A*	Moment Arm (mm)	Mass Flow (g/s)	Exit Area (mm^2)	Average Velocity (m/s)	% Variation From Average	Standard Deviation (m/s)
CC-R8-H0.5	0.06	243	4.1	100	37.99	37.67	5.35
CC-R4-H0.5	0.12	271	4.1	100	34.76	15.31	1.80
CE-A8-B4-H0.5	0.12	274	4.1	100	34.84	14.16	1.68
CE-A16-B8-H0.5	0.03	249	4.1	100	36.59	38.49	5.38
CB-R8-H0.5	0.06	284	4.1	100	36.63	10.11	1.31
CB-R16-H0.5	0.03	272	4.1	100	38.27	27.45	3.55
CH-R8-H0.5	0.06	279	4.1	100	35.85	28.20	3.38

For the discrete and fluidic actuator ID classification in Table 5, the first character "D" signifies that the design is a discrete slot actuator, and "F" signifies the design is a fluidic oscillator design. The second ID character represents the Coanda profile shape which is "C" for all designs that are circular in profile. The second set of characters begins with "W" followed by the exit slot width measurement in mm. The third set of characters begins with "S" followed by the slot spacing—sealed-off distance between AFC exit slots—measurement in mm. As with the continuous slot designs, the final set of characters begins with "H" followed by the slot height measurement in mm. All discrete slot actuators followed the same external profile and thus had a moment arm equal to that of the baseline design (ID CC-R8-H0.5).

Table 5: Characteristics of discrete slot actuators with *r*=8mm.

Actuator ID	*h/r*	Mass Flow (g/s)	Moment Arm (mm)	Exit Area (mm^2)	Average Velocity (m/s)	% Variation From Average	Standard Deviation (m/s)
FC-W2-S40-H1.0	0.12	1.0	239	10	91.60	21.55	6.73
FC-W2-S20-H1.0	0.12	2.0	239	20	85.48	18.23	4.83
DC-W2-S20-H0.5	0.06	1.0	243	10	93.86	6.09	1.68
DC-W4-S20-H0.5	0.06	2.0	243	20	85.90	11.95	2.87
DC-W2-S20-H1.0	0.12	2.0	239	20	94.76	1.98	0.55
DC-W8-S20-H0.5	0.06	4.1	239	40	87.41	6.83	2.04
DC-W4-S20-H1.0	0.12	4.1	239	40	91.38	6.98	2.30

An example configuration is depicted in Figure 12, which represents the baseline actuator profile. Note that the baseline actuator used in the varying AFC configuration studies was equal in external geometry to the 200mm actuator used in the varying spanwise location testing and both were continuous 2D slot actuators. However, the baseline actuator ID CC-R8-H0.5 for varying configuration testing was a separate physical device which was printed with one less diffusion grid inside its plenum compared to Figure 12. Thus, these two actuators varied slightly in exit slot velocity characteristics and overall performance despite sharing the same external profile and continuous slot nozzle type.

Each actuator was 200mm in length and was additively manufactured with PLA. A ¼ inch NPT thread was designed at each end of the model to facilitate the air supply hose connection. An internal plenum with a perforated sheet was used to evenly distribute

the flow over the exit area. Due to this manufacturing process, the fluidic oscillators were examined using a hotwire and Fast Fourier Transform (FFT) analysis to identify dominant frequencies. The actuator ID FC-W2-S20-H1.0 had ten fluidic oscillators, nine of which performed their intended function as sweeping jets and one did not oscillate due to defective manufacturing, so it performed as a discrete jet. The actuator FC-W2-S40-H1.0 had five fluidic oscillators, four of which performed as sweeping jets (one failing to oscillate). Thus, the FO actuators in this study performed with 90% and 80% sweeping jet effectiveness, respectively.

2.1.3 Test Conditions

The following two subsections will describe the testing conditions and test matrices used to evaluate the Coanda actuators in these experiments. Section 3.1.3.1 will describe the test conditions of evaluating the effect of AFC spanwise location in the propeller slipstream and section 3.1.3.2 will describe the test conditions of evaluating AFC configuration variations. All testing for the experiments described was conducted on the static test stand in Figure 9.

3.1.3.1 Varying Spanwise AFC Location Conditions

To determine the effect of actuator spanwise location, each trailing edge segment was 100mm (0.52*R*) in span, with two Coanda actuator segments of 200mm (1.05*R*) and 100m (0.52*R*) respectively. The two Coanda actuators were each evaluated for exit slot

velocity uniformity, load generation, and per-span blowing cost in the form of momentum coefficient.

The 200mm actuator was designed and fabricated—3D printed with PLA—first, and the 100mm actuator was subsequently developed to test the effect of AFC at more refined AFC spanwise location increments. This allowed for multiple locations and spanwise AFC sizes to be examined. The test matrix to evaluate different spanwise locations of the 200mm AFC section is displayed in Table 6, and Table 7 displays the test matrix for the varying spanwise location of the 100mm AFC section.

Force and moment data from the load cell were examined with AFC located at these different spanwise locations for four AFC mass flow rates supplied by an Alicat mass flow controller rated for 40g/s (1000slpm) of mass flow with no freestream velocity—the upstream propeller was the only momentum source. Moments were measured about the quarter chord, base location of the load cell in this setup. Note that the mass flow rate of 2g/s for the 200mm AFC—corresponding to 1g/s for 100mm AFC—was bypassed because preliminary testing demonstrated that loads generated by this setpoint were of too small a magnitude to be registered by the load cell. Once a steady state 6000 RPM was reached, load cell data were collected at each test condition for 10 seconds at a recording rate of 25kHz.

Table 6: Test matrix for 200mm AFC spanwise locations at 6000 RPM.

Spanwise Coanda Actuator Location	Data Collection Mechanism	Data Collected	Mass Flowrate (g/s)
-1.05*R* : 0.00*R*	6DoF Load Cell	L (N), M_z (Nm)	0, 4, 6, 8
-0.63*R* : +0.42*R*	6DoF Load Cell	L (N), M_z (Nm)	0, 4, 6, 8
-0.52*R* : +0.52*R*	6DoF Load Cell	L (N), M_z (Nm)	0, 4, 6, 8
-0.42*R* : +0.63*R*	6DoF Load Cell	L (N), M_z (Nm)	0, 4, 6, 8
0.00*R* : +1.05*R*	6 DoF Load Cell	L (N), M_z (Nm)	0, 4, 6, 8

Table 7: Test matrix for 100mm AFC spanwise locations at 6000 RPM.

Spanwise Coanda Actuator Location	Data Collection Mechanism	Data Collected	Mass Flowrate (g/s)
-1.05*R* : -0.52*R*	6DoF Load Cell	L (N), M_z (Nm)	0, 2, 3, 4
-0.52*R* : 0.00*R*	6DoF Load Cell	L (N), M_z (Nm)	0, 2, 3, 4
-0.26*R* : +0.26*R*	6DoF Load Cell	L (N), M_z (Nm)	0, 2, 3, 4
0.00*R* : +0.52*R*	6DoF Load Cell	L (N), M_z (Nm)	0, 2, 3, 4
+0.52*R* : +1.05*R*	6DoF Load Cell	L (N), M_z (Nm)	0, 2, 3, 4

3.1.3.2 Varying AFC Geometry Conditions

For experiments which involved varying AFC geometric configuration, 14 different Coanda actuators with 200mm (1.05*R*) span were 3D printed with PLA and tested on the static test stand. Like the varying AFC location tests, these 14 Coanda

actuators were each evaluated for exit slot velocity uniformity, load generation, and per-span blowing cost in the form of momentum coefficient. The spanwise location of Coanda AFC actuators in this testing was held constant at the center-span -100mm to +100mm location (-1.05*R*:+1.05*R*), as well as the trailing edge configuration of the wing setup. The test matrix to evaluate different geometric configurations of the 200mm AFC section is displayed in Figure 9.

Force and moment data were examined for four AFC mass flow rates—0, 4, 6, and 8 g/s—supplied by an Alicat mass flow controller. Like the varying AFC spanwise location testing, there was no freestream velocity—the upstream propeller was the only momentum source. Moments were measured about the quarter chord, base location of the load cell in this setup. Once a steady state 6000 RPM was reached, load cell data were collected at each test condition for 10 seconds at a recording rate of 25kHz.

2.2 Data Analysis Methods

The focus of data collected in these studies was the lift force and pitching moment generated by AFC, as well as the AFC blowing cost per unit span characterized as momentum coefficient and the local momentum flux along a set spanwise wing section. Force and moment data collected in this study were tared with the baseline 0g/s and 6000 RPM to measure the effects of TE Coanda AFC as compared to the no-AFC operating condition. Lift, pitching moment, and momentum coefficients were nondimensionalized using approximations to accommodate the hover flight testing condition and the fixed span of TE AFC actuators used for testing. Note that the nondimensionalization

convention presented here is updated from the convention presented in the SciTech 2024 conference papers written by the same author of this present work [34], [35].

2.2.1 Force and Moment Nondimensionalization

Since these experiments involved a setup with no freestream velocity, the propeller induced velocity (U_i) was used as the characteristic velocity to nondimensionalize variables in the hover case of the present study. Shown in Eq. (5), induced velocity is a function of the thrust generated by the propeller (T), ambient density (ρ), and propeller radius (R) [36]. Note that the induced velocity was a constant U_i=8.5m/s for the setpoint of 6000RPM maintained for the AFC load evaluation tests in this work. This induced velocity value was computed using thrust data—force data in the x-axis—collected from the 6DoF load cell when the T-Motor propeller was spun up to a constant setpoint of 6000RPM.

$$U_i = \sqrt{\frac{T}{2\rho\pi R^2}} \tag{5}$$

Another variable used for nondimensionalization was the AFC reference area (S_{AFC}) which involves the multiplication of the AFC spanwise measurement (b_{AFC}) and the full wing chord (c) and is presented in Eq. (6). This reference area varies from the traditional full wing reference area by using the AFC span rather than the wingspan measurement to more accurately characterize where the TE Coanda actuators are most

effective in the propeller slipstream since the AFC actuators did not span the entire trailing edge.

$$S_{AFC} = b_{AFC} * c \tag{6}$$

The lift and pitching moment coefficients in this study utilize this slipstream velocity in place of freestream velocity and are given as Eq. (7) and Eq. (8) respectively. In these equations, C_L and C_m represent the lift and pitching moment coefficients while L and M_z represent the dimensional lift force and pitching moment. The ambient density (ρ_{amb}) and wing chord (c) remained unchanged from the conventional lift and pitching moment coefficient equations.

$$C_L = \frac{L}{\frac{1}{2}\rho_{amb}(U_i)^2 S_{AFC}} \tag{7}$$

$$C_m = \frac{M_z}{\frac{1}{2}\rho_{amb}(U_i)^2 S_{AFC} * c} \tag{8}$$

2.2.2 Momentum Coefficient Nondimensionalization

The momentum coefficient, C_μ, was computed using the AFC exit slot velocity (U_{AFC}) approximation shown in Eq. (9), with the full relation displayed in Eq. (10). The reference area used in the denominator of the AFC velocity formula was the AFC span (b_{AFC}) multiplied by the design value of exit slot height, (h). The definition of momentum coefficient for the AFC test cases in this study also used the length of actuators as the reference span in the denominator rather than the full wingspan. Thus, C_μ is a cost per unit span for each actuator in the present work which defines the efficiency of actuation. The numerator includes the mass flow rate supplied by AFC actuators ($\dot{m}_{AFC}$), as well as the exit slot velocity of air supplied to the AFC (U_{AFC}). The denominator includes the wing chord and span of Coanda actuators, as well as the ambient density and propeller induced velocity (U_i).

$$U_{AFC} = \frac{\dot{m}_{AFC}}{\rho_{amb} b_{AFC} h} \tag{9}$$

$$C_\mu = \frac{\dot{m}_{AFC} U_{AFC}}{\frac{1}{2}\rho_{amb}(U_i)^2 S_{AFC}} \tag{10}$$

2.2.3 AFC Placement Assessment

Optimal AFC placement was assessed relative to the local propeller slipstream momentum shown in Eq. (11). This equation represents the momentum flux per unit span

for an AFC actuator. This is computed by multiplying ambient density (ρ_{amb}) by the integral of velocity squared over the actuator spanwise length. This integral is also equal to the summation of the measured slipstream velocity experienced ($U_{ss,y}$) squared in the spanwise *y* direction—beginning at location y_1 and ending at spanwise location y_2—divided by the actuator span (b_{AFC}). This J_{ss} parameter eliminates the dependence on AFC span and relates the moment only to local momentum flux. In this study, density was assumed to be constant and equal for both the freestream and AFC flow. With constant density, summing the square of slipstream velocity measurements at the 75% chord location characterizes the momentum flux (J_{ss}) over the wing experienced at each AFC spanwise location.

$$J_{ss} = \rho_{amb} \int_{y_1}^{y_2} (U_{ss,y})^2 dy = \frac{\rho_{amb}}{b_{AFC}} \sum_{y=y_1}^{y_2} (U_{ss,y})^2 \, \Delta y \tag{11}$$

Chapter 3. Results and Discussion

First, the velocity profile development along the wing is discussed, with a focus on the spanwise profile at the 75% chord location where AFC and traditional deflections are placed. Next, changes to nondimensional pitching moment and lift coefficients are explored for trailing edge Coanda actuator locations of 200mm and 100mm actuators, respectively.

Finally, discussion is conducted which examines the overlap and correlation between trailing edge velocity profile and Coanda actuator effectiveness for the case of propeller-driven flow which simulates an aircraft in hover flight.

3.1 Trailing Edge Velocity Profile

The first component of this study involved characterizing the propeller slipstream velocity. To accomplish this, both qualitative and quantitative analysis methods were used. Surface oil flow visualization (SOFV) was used to qualitatively capture the propeller slipstream development along the wing and a Kiel probe traverse survey was conducted to quantifiably validate and characterize the SOFV findings.

3.1.1 Propeller Slipstream Flow Visualization

SOFV was first performed with fluorescent green Day-Glo powder and oil spread along the wing's surface with no injected flow from the AFC actuators and a 0-degree deflection. Figure 17 displays the SOFV results which depict the propeller slipstream and its contraction along the wing. For this flow visualization, the wing was mounted

horizontally to minimize gravitational effects on oil dispersion. The propeller was located at the top of the image and pushed flow back over the wing. Dashed black lines were added based on a qualitative assessment of the slipstream boundaries. Testing was performed for propeller spinning in the clockwise and counterclockwise directions—when viewed from downstream to upstream. The asymmetry about the propeller centerline is dependent on the direction of propeller rotation—always skewed toward the downwash or impinging side of the wing which experiences the descending propeller blade. Additionally, the propeller slipstream contracted by 20% such that the span measurement of the slipstream at the trailing edge of the wing was 80% of the propeller diameter of 381mm ($2R$). This indicates that at the wing's trailing edge, the slipstream has not achieved the full contraction of 30% expected for hover flight based on momentum theory [37]. This expected contraction is based on the assumed area of a fully contracted cross-sectional wake area—also referred to as the vena contracta—to be 50% of the original rotor disk area based on ideal fluid flow assumptions [36]. The ratio of the contracted wake radius to the rotor radius then becomes $R/\sqrt{2} = 0.7R$; 70% of the original radius yields a contraction of 30%.

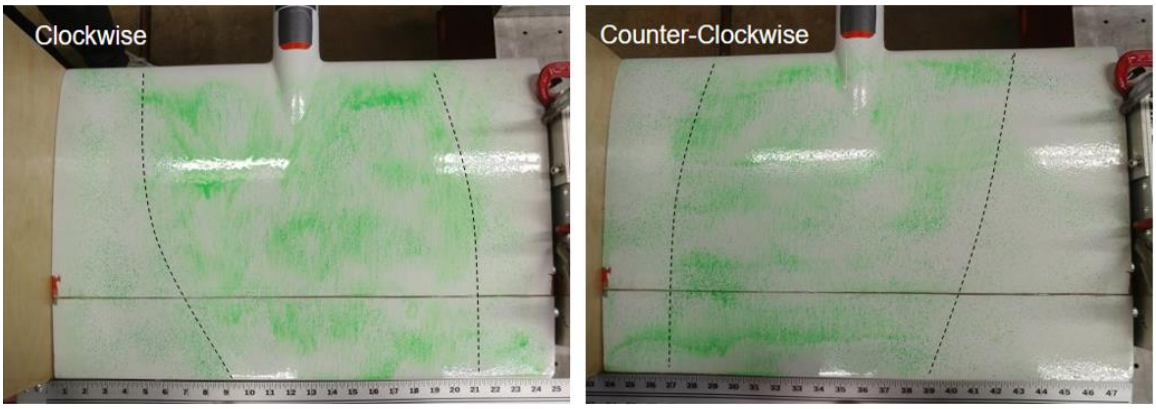

Figure 17: Flow visualization for clockwise and counterclockwise propeller rotation at 7000 RPM and 0.208m (1.09*R*) standoff distance upstream of the wing.

3.1.2 Propeller Slipstream Survey Measurement

To quantitatively measure the velocity profile along the wing, a traverse survey was conducted with a Kiel probe 10mm off the surface of the wing—to remain outside the boundary layer of 8mm—with the propeller running at a constant RPM and no injected flow to the AFC. This boundary layer height was acquired using a hooked pitot static probe designed for boundary layer measurements which was traversed in 1mm *z*-axis increments at the three spanwise locations of -*R*, +*R*, and 0*R* (center span) along the *y*-axis and 0.5*c* *x*-axis position of the wing. The boundary layer was measured at these locations to ensure the propeller wake was captured and the flow was attached. The boundary layer height was 7mm at the -R and +R locations, and 8mm at the 0R location, thus the 8mm boundary layer height estimation along the wing planform was made. Figure 18 shows data from a Kiel probe velocity survey collected at five chordwise locations and 30 spanwise locations (450 locations total) to provide a full wing velocity

profile map. A pressure transducer measured the total pressure, and each location was sampled at a rate of 25kHz for 2.5 seconds. The velocity profile along the trailing edge was then calculated using the total pressure data gathered by the Kiel probe in combination with the ambient density and pressure at the time of experimentation. Although the streamlines contraction along the wing planform indicated a pressure decrease within the flow field, the average value of ambient pressure at the time of each test was used as a constant static pressure for computations.

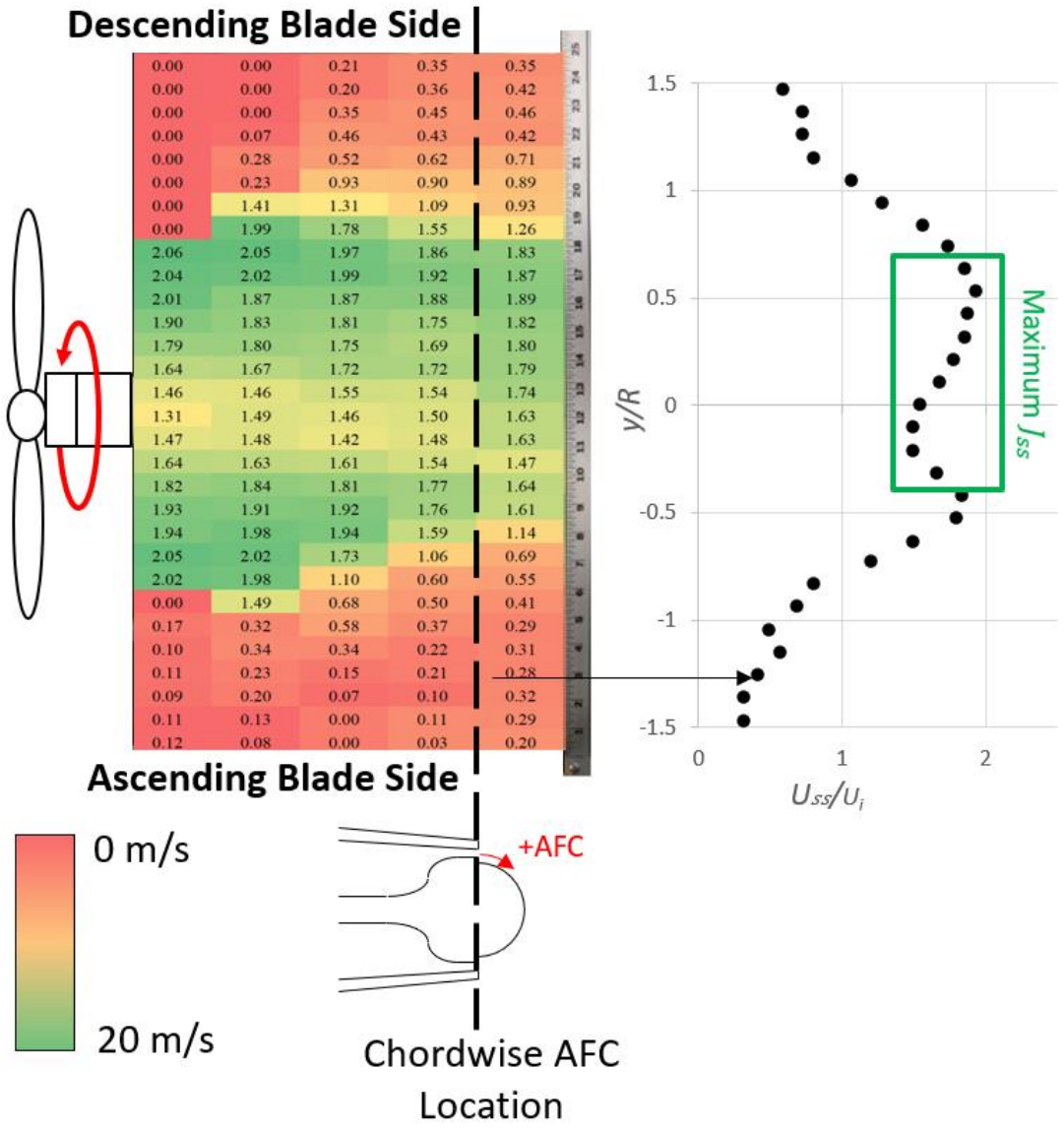

Figure 18: Velocity heat map for clockwise propeller rotation at 7000 RPM, nondimensionalized by induced velocity (U_i=10.7m/s) as measured by a pitot-static probe through chordwise and spanwise traverse surveys.

The results of this velocity survey numerically validate the chordwise slipstream contraction dependence on the propeller rotation direction. The rightmost segment of

Figure 18 also includes a plot of the velocity profile experienced at the 75% chord location and identifies the region of maximum span-averaged momentum flux, J_{ss}. The computation of J_{ss} was achieved by summing the local velocity squared over 200mm regions, then dividing by the spanwise AFC length, as shown in Eq. (11); this J_{ss} was the primary metric used for determining test locations of TE Coanda AFC for both the 100mm and 200mm Coanda AFC actuator lengths. The purpose of designing the varying spanwise location test matrices in Table 6 and Table 7 was to examine if this green-boxed location of maximum J_{ss} at $0.75c$ would correspond to the location of maximum control authority—evaluated as pitching moment generation—and examine if lower J_{ss} locations would correspond to degraded control authority with less propeller slipstream momentum supplied for AFC flow entrainment.

3.1.3 Literary and Theoretical Comparison

The findings from this slipstream velocity investigation have been observed by other aerodynamicists who credited this asymmetry to the propeller-wing interactions. Witkowski et al. in 1989 experimentally observed that when supplied by a propeller-driven momentum source and low freestream flow, the spanwise lift distribution over a wing was asymmetric with a bias toward the side of the wing which experiences a descending propeller blade [38]. Subsequently in 1991, Johnson et al. identified the source of this rotation-dependent lift distribution along the wingspan was due to the wing splitting the propeller's single rotating vortex into two counter-rotating vortices, each biased towards the side of the wing on which the propeller blade descends [33].

Furthermore, Johnson et al. observed that each counter-rotating vortex had a spanwise velocity component which was positive in the direction of the descending propeller blade.

More recent studies have characterized the factors which can impact the propeller slipstream skew. Deters et al. in 2015 conducted a study of propeller-wing interactions using propellers with varying geometric parameters—different airfoil shape, diameter, and pitch values—and found that the magnitude of slipstream velocity was dependent on propeller geometry, but the static slipstream skew remained peaked at the same relative location with maximum velocity initially occurring at 75% the propeller radius—when measured from the ascending blade side of the wing—and contracting towards the center but remaining skewed 50% towards the descending propeller blade [37]. In other words, the propeller slipstream was consistently skewed at least 0.5R toward the descending blade side due to the presence of the wing because of the vortex splitting and spanwise migration.

In the present work, the location of maximum propeller slipstream velocity at the wing trailing edge was measured to be between the spanwise locations of 0.5R and 0.6R skewed toward the descending propeller blade. Thus, the findings from previous researchers of propeller-wing interactions corroborate the findings from measurements which support this thesis. Additionally, these findings from literature help inform this work by explaining the physical vortex-splitting phenomenon which causes the propeller slipstream skew so this feature can potentially be used for aerodynamically advantageous TE Coanda AFC placement.

3.2 Varying AFC Spanwise Location

Once the trailing-edge velocity profile with no AFC and 0 degrees of deflection was characterized, the trailing edge was interchanged for different configurations of Coanda actuator sections with blank sections, which match the geometry descriptions outlined in section III. The tests, detailed in Table 6 and Table 7 of Section III, were conducted for the 200mm and 100mm AFC actuator sections, respectively.

This section of the results will present and explain the data collected from testing the two Coanda actuators of equal internal geometry and external profile at five different spanwise locations along the wing trailing edge of the tabletop static test stand. These results will be presented first as nondimensionalized lift force and pitching moment effect versus mass flow injection, then as nondimensionalized lift force and pitching moment versus AFC blowing cost per unit span, represented as momentum coefficient. This results section will include a discussion comparing values achieved by this study with existing literature detailing similar experiments with Coanda actuators.

3.2.1 Pitching Moment and Lift Force vs. Mass Flow

The nondimensionalized pitching moment and lift force data collected from the tabletop load cell during the Coanda actuator operation are displayed in Figure 19 and Figure 20. The pitching moment coefficient results in Figure 19 demonstrate that the optimal location for AFC in terms of pitching moment benefit is the location of the highest trailing edge velocity. This location, corresponding to the blue line in the following two figures, is defined as $0.00R$:$+0.52R$ for the 100mm actuator and –

0.42*R*:+0.63*R* for the 200mm actuator. Additionally, the pitching moment results for the two actuators of different lengths demonstrate that the propeller slipstream is more sensitive to the 100mm actuator placement since it shows an improvement of 20% compared to the other four locations tested, whereas the optimally placed 200mm actuator out-performs the other three central locations by 5-7%. The testing with 100mm actuator placement provides evidence that placing AFC in the region of maximum velocity in the propeller slipstream at 0.75*c*—shifted slightly towards the downwash side in this case—yields the greatest pitching moment performance. Note that the 100mm actuator with 4g/s supplied produces ΔC_m comparable to that of the 200mm actuator at 8g/s because their exit slot velocities are equal at these respective mass flow injections.

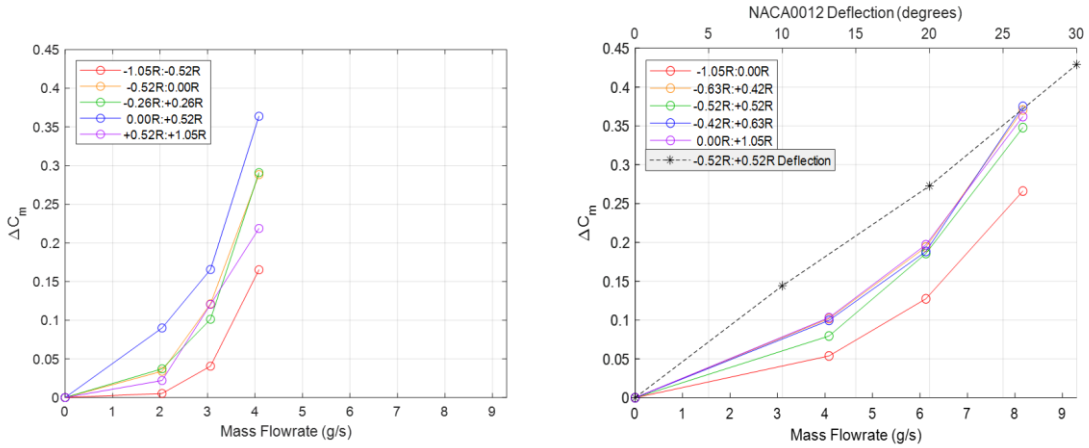

Figure 19: ΔC_m vs. mass flow at 6000 RPM and varying spanwise location for 100mm (0.52*R*) AFC on the left and 200mm (1.05*R*) AFC on the right.

With an AFC length of approximately 50% of the propeller radius, control authority is maximized by placing the trailing-edge Coanda actuator in a location starting at the center and extending approximately 50% of the propeller radius onto the downwash side. The improvement is slight for an AFC actuator of approximately equal span to the propeller radius, but still demonstrated maximum control authority when placed with 60% span on the propeller downwash side of the wing.

Additionally, the data from the Coanda actuator operation demonstrate that the furthest AFC placement on the upwash side of the propeller slipstream leads to degraded control performance. This location, corresponding to the red line in the following two figures is defined as -1.05*R*:-0.52*R* for the 100mm actuator and –1.05*R*:0.00*R* for the 200mm actuator. The AFC at this location produces pitching moments significantly lower than three more central locations at all mass flow rates tested. Thus, AFC produces the lowest pitching moment performance when placed in the region of lowest velocity in the profile at 0.75*c*, supporting the theory that AFC control performance correlates directly with the propeller slipstream velocity profile.

Examining the lift coefficient results in Figure 20, the most optimal AFC section placement for lift performance appears to be the center-span location. This does not exactly match the results acquired from the pitching moment analysis, where the optimal location was skewed towards the downwash side of the wing, but the performance in lift at the three most central locations is still greater than that of the two locations on the outer edges of the propeller slipstream. This indicates that the lift measurement of this test stand is not impacted as significantly as pitching moment by some aerodynamic

phenomena, such as the trailing-edge flow turning angle. The flow turning angle at the trailing edge is greatest for AFC in the exact region of highest velocity towards the downwash side, and this angular change in the load cell *z*-axis impacts the *z*-axis pitching moment measurement more significantly than lift which is measured as the *y*-axis force over the entire wing. If AFC is being placed along the trailing edge of a wing to improve lift performance, the center-span location is sufficient.

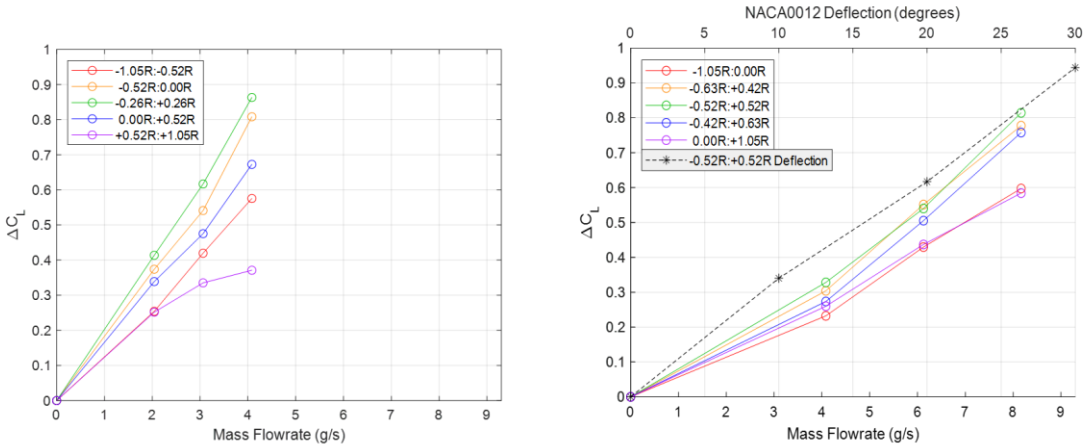

Figure 20: ΔC_L vs. mass flow at 6000 RPM and varying spanwise location for 100mm (0.52*R*) AFC on the left and 200mm (1.05*R*) AFC on the right.

Furthermore, the force and moment data were compared to a conventional 200mm control surface deflection which was placed at the center-span (-0.52*R*:+0.52*R*) of the wing with the same hinge point on the wing as the AFC actuators. With this deflection piece attached, the remainder of the wingspan maintained the same blank geometry as was used when testing the center-span 200mm actuator. This deflection piece followed the NACA 0012 profile, and the angle of deflection was altered from 0 degrees to 30

degrees using 3D-printed spacer pieces to maintain a constant angle while running the propeller test stand. The traditional deflection corresponds to the black dashed line in Figure 19 and Figure 20. These figures demonstrate that the 200mm Coanda AFC actuator produced ΔC_m=0.11 at 4g/s, which was the estimated ΔC_m from 7° deflection, and ΔC_m=0.38 at 8g/s, which was the estimated ΔC_m from a 27° deflection at 8g/s. The ΔC_L=0.32 at 4g/s from the 200mm AFC actuator was equal to ΔC_L from a 10° deflection and the ΔC_L=0.82 at 8g/s corresponded to the estimated ΔC_L from a 26° deflection.

The lift and pitching moment both increased following a linear trend when altering the deflected section, whereas the effect of AFC increased following a quadratic trend for the pitching moment and a linear trend for the lift coefficient. The quadratic ΔC_m trend with AFC could be explained by the *z*-axis moment measurement of the load cell being heavily influenced by flow entrainment and direction alteration at the wing's trailing edge. The Coanda jet is an active flow control device that both redirects momentum from the entrained slipstream and adds momentum to the flow, and the flap deflection is a passive flow control device that only redirects momentum. Therefore, as the mass flow exiting the TE Coanda AFC actuator increases, the momentum flux—which produces positive ΔC_m—increases at a greater rate than that of the flap deflection which causes this difference in trends.

Additionally, this increased momentum flux combines with stronger Coanda jets to turn the flow more at greater injection mass flow rates. This effectively wraps the TE flow greater than 90°, a phenomenon which can be qualitatively verified by tuft flow visualization and passing one's hand along the trailing edge. This flow wrapping angle

has been measured by the Coanda surface in the present study (h/r=0.062) to be approximately 140° at all mass flow rates in the condition of no upstream flow source. The increased flow wrapping by TE Coanda AFC does not occur with a traditional control deflection which is conventionally tapered to match the wing's airfoil profile for drag reduction.

The quadratic trend of pitching moment with increasing mass flow indicates that if higher injection mass flow rates were to be tested, the pitching moment effect of AFC could surpass that of a traditional control surface of the same span. In testing for this experiment, mass flow was limited by the back pressure supply and materials used. Supplying 8g/s required a back pressure of 40 PSI—measured by the mass flow meter—for 200mm (1.05R) AFC. The setpoint of 8g/s was not exceeded due to the possibility of damaging the fine internal diffusion grids or bursting the part from excessive internal pressure inside the 3D-printed PLA actuator, which occurred in preliminary testing.

3.2.2 Momentum Coefficient Per-Span Cost Analysis

Displayed in Figure 21 and Figure 22 are plots of the pitching moment coefficient and lift coefficient versus momentum coefficient curves for the AFC actuator locations tested in this study. Eq. (10) shows the C_μ defined for the hover flight case, using the propeller induced velocity in place of the freestream velocity typically present in the equation. For the same C_μ, the 200mm actuator performs near equal to the 100mm actuator in terms of force and moment generation when located within the propeller slipstream. Although the ΔC_L and ΔC_m are greater at most optimal spanwise placement

for the shorter-span actuator based on mass flow injected, this momentum coefficient analysis clearly demonstrates that the 100mm actuator is equally as costly to operate as the 200mm actuator, while providing the same lift and pitching moment benefit for all locations on the downwash side of the wing which enable the propeller slipstream to be entrained by AFC.

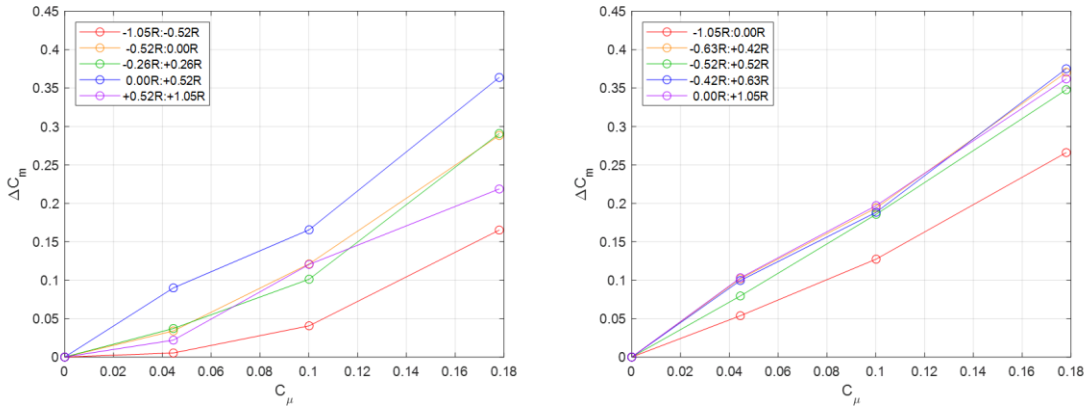

Figure 21: ΔC_m vs. C_μ at 6000 RPM and varying spanwise location for 100mm (0.52R) AFC on the left and 200mm (1.05R) AFC on the right.

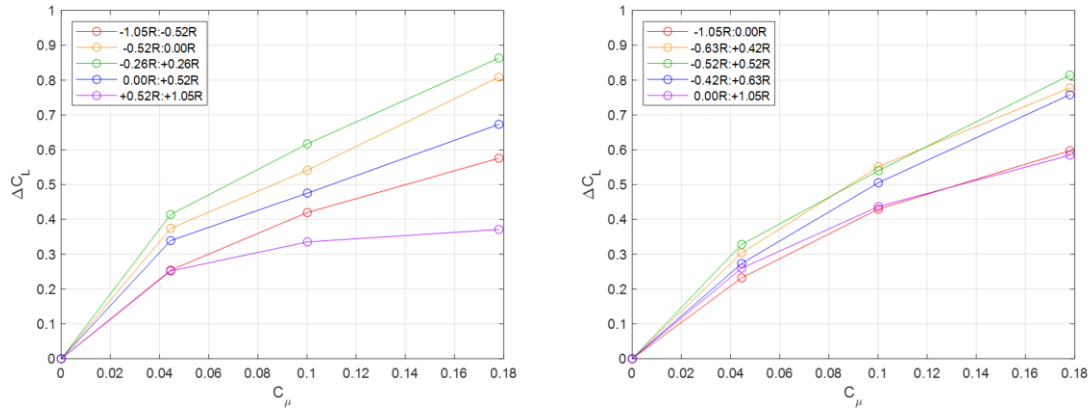

Figure 22: ΔC_L vs. C_μ at 6000 RPM and varying spanwise location for 100mm (0.52R) AFC on the left and 200mm (1.05R) AFC on the right.

The ΔC_L vs. C_μ curve for the 200mm actuator follows the same trend and relative values as the work of other aerodynamicists who have developed and tested Coanda AFC actuators in recent years. Warsop and Crowther in 2018 documented results from a Coanda actuator on the DEMON aircraft with a circular profile and h/r=0.067 with h=0.2mm and r=3mm. This DEMON aircraft design achieved a maximum ΔC_L=0.14 with a momentum coefficient of C_μ=0.017, yielding a dC_L/dC_μ=8 at this maximum setpoint and freestream velocity of 20m/s—2.5 times greater than the U_i=8.5m/s in the present work—and dC_L/dC_μ>30 at lower blowing rates [6]. The dC_L/dC_μ achieved by the 100mm continuous AFC Coanda actuator at center-span in this study was 4.8 at the maximum injection flow setpoint and dC_L/dC_μ=9.8 at the lowest blowing rate. Despite this lower dC_L/dC_μ performance compared to the DEMON aircraft, the 100mm and 200mm Coanda actuators in the present study achieved a ΔC_L over four times greater in magnitude than the DEMON aircraft.

The Coanda AFC designs in the present study used a similar h/r=0.062 but h and r were scaled up in dimension from the DEMON aircraft by a factor of 2.67. This scaling difference combined with the differences in velocity source and injection flow (C_μ) magnitudes were likely causes for performance differences from the Coanda actuators in this study. Comparison between the DEMON aircraft performance indicates that although force generation was greater, there is room for improvement in terms of dC_L/dC_μ for this study's Coanda actuator design.

Similarly, Henry and Williams tested a Coanda actuator with h/r=0.05 which achieved a change in lift coefficient of 0.3 at a momentum coefficient of 0.025, yielding a dC_L/dC_μ=11 at this maximum blowing setpoint and dC_L/dC_μ=15 at lower blowing rates [25]. The Coanda actuators in Henry and Williams' study were sweeping jets and testing was conducted in a wind tunnel with freestream velocities of up to 28 m/s. Although a direct comparison cannot be made to the present study, it is useful to understand that with a similar h/r=0.062, the Coanda AFC actuator in the present study yielded consistently lower dC_L/dC_μ values than in existing literature, further indicating that blowing efficiency improvements are possible.

3.2.3 Control Authority Relation to Propeller Slipstream

Next, the loads experienced by the propeller-wing setup with AFC blowing at each location were overlayed on the velocity profile at the 75% chord location. Displayed in Figure 23 are the nondimensional pitching moment results overlayed on their respective spanwise locations with horizontal bars representing the spanwise location of AFC which produced the moment. This figure shows that pitching moment—the measure of control authority targeted by the TE Coanda AFC in this study—is dependent on slipstream velocity (as expected).

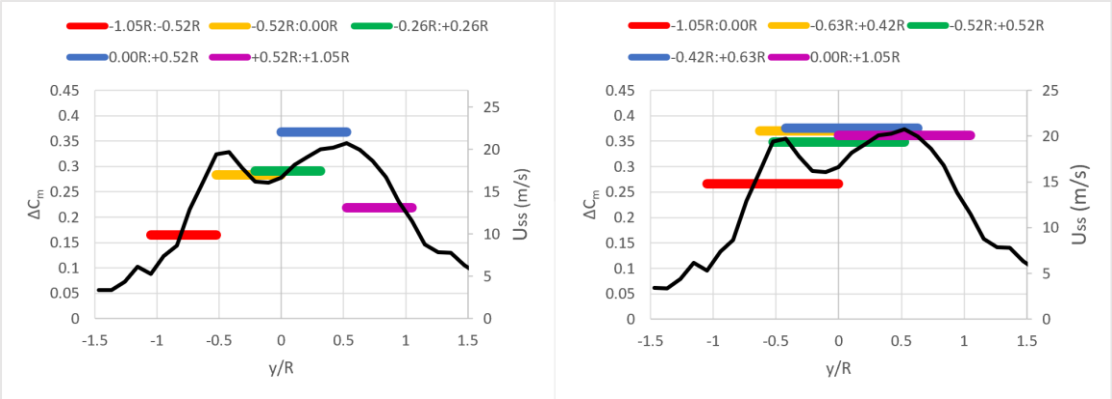

Figure 23: ΔC_m produced at Coanda actuator locations—100mm (0.52*R*) with 4g/s blowing on the left and 200mm (1.05*R*) with 8g/s blowing on the right—overlayed on U_{ss} profile at 0.75*c*.

This relation to slipstream velocity measured at the chordwise location of AFC was not replicated by the lift data, which is shown comparably in Figure 24. This is likely due to the way that lift is measured as a force over the wing's surface (from the quarter-chord location to the trailing edge in this setup) and is largely affected by the velocity profile that occurs along the wing before the 75% chord location and only slightly affected by AFC placed at the trailing edge. The magnitudes of lift measured in this study were on the order of 3-4N while the pitching moment magnitudes were on the order of 0-1Nm. Thus, the lift force measurement is less sensitive to TE AFC placement and more dependent on the velocity profile over the entire wing. The TE AFC placed in optimal spanwise locations could have also produced a pure moment when entraining higher velocity flow, which is only represented in the pitching moment measurements and not the lift measurements in this experiment.

Another reason for the C_L and C_m data not yielding the same performance at the same TE AFC locations is that the load cell placed at 0.25*c* may not be the aerodynamic center of the airfoil when AFC is actuated. The NACA 0012 itself is a symmetric, thin airfoil with an aerodynamic center at 0.25*c*, but AFC actuation at the trailing edge of the wing may produce an effective camber. An effective camber would move the aerodynamic center further aft on the airfoil which could be the cause of discrepancy between the lift and pitching moment measurements on this setup for AFC testing. Camber on an airfoil inherently improves the lifting performance compared to the un-cambered airfoil state which was present in the tare of each data point. The presence of an effective camber is likely the cause of lift and pitching moment not aligning as expected because it would affect lift measurements in this setup.

Overall, lift performance is still improved by the addition to TE AFC actuators, but not as sensitive to AFC placement as pitching moment. The discrepancy between lift and pitching moment is not of major concern because both show improvements when placed within the propeller slipstream bounds compared to AFC locations which do not capture the 0.75*c* propeller slipstream profile peaks. Additionally, pitching moment is the parameter of greater interest due to focus of these TE AFC actuators being control authority for the tail-sitting VTOL vehicle design.

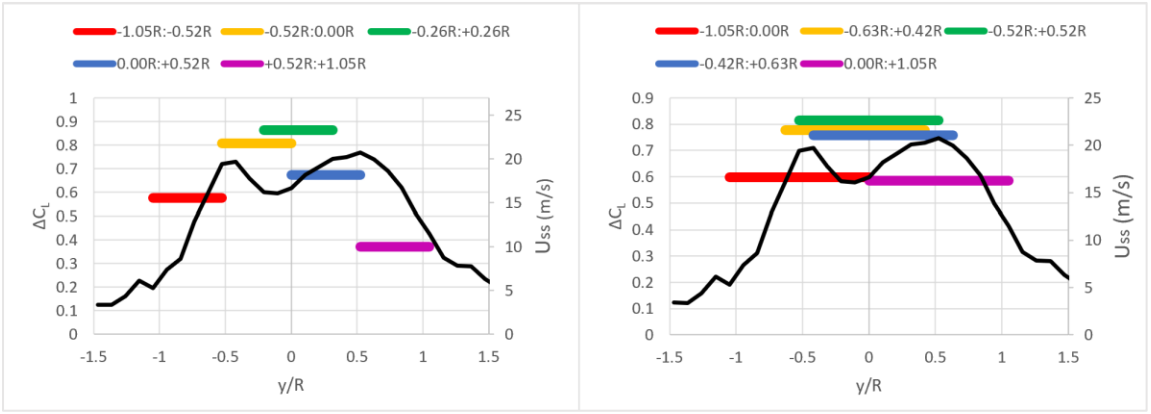

Figure 24: ΔC_L produced at Coanda actuator locations—100mm (0.52R) with 4g/s blowing on the left and 200mm (1.05R) with 8g/s blowing on the right—overlayed on U_{ss} profile at 0.75c.

When the slipstream velocity—the black curve in Figure 23—is integrated over the spanwise region of actuator location as shown in Eq. 11, the result becomes momentum flux per unit span experienced at each actuator. Shown in Figure 25 is the strong correlation between pitching moment coefficient and momentum flux per unit span, J_{ss}, over the region of TE AFC effectiveness for both actuators at each spanwise position evaluated. This further demonstrates that placing TE AFC at regions of greater velocity—and momentum flux—on a wing will lead to increased pitching moment and thus increased control authority. Furthermore, this plot establishes a linear relationship between pitching moment coefficient and slipstream momentum flux per unit span such that the value of pitching moment change (ΔC_m) can be approximated by multiplying a known J_{ss} by a factor of 8.59×10^{-4} for the 200mm Coanda actuator with circular profile and h/r=0.062, and a factor of 6.87×10^{-4} for the 100mm actuator of the same profile and

wing installation. The linear fit through the ΔC_m vs J_{ss} data for both actuator spans yields R^2>0.99, verifying that a linear approximation accurately describes these data.

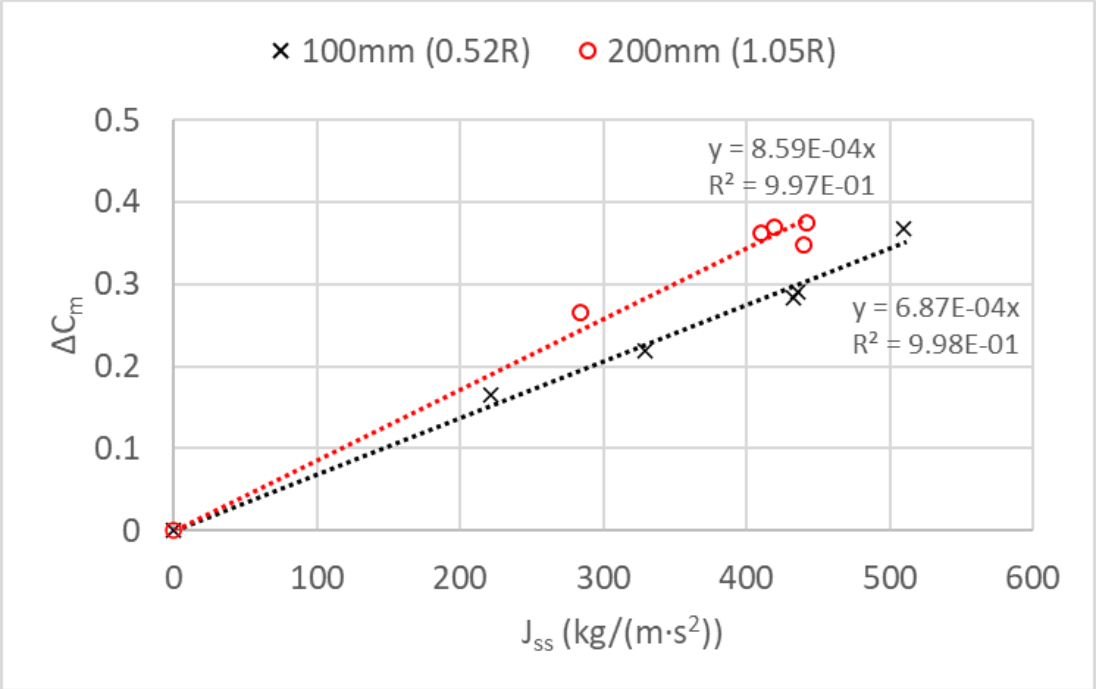

Figure 25: Linear relationship of ΔC_m vs. J_{ss} for all TE AFC locations.

The presence of a linear relationship was established using data from both TE Coanda AFC actuators of varying length—100mm (0.52*R*) and 200mm (1.05*R*). This indicates that the linear relationship will hold true for TE Coanda AFC actuator lengths, but each actuator will have a slightly different ΔC_m vs J_{ss} slope. Although manufactured

using the same material, fabrication methods, internal plenum geometry, external Coanda surface geometry, and with the same wing trailing-edge configuration, the ΔC_m vs J_{ss} slopes for these circular Coanda actuators with r=8mm and h=0.5mm were close in value but not equal. There was a 22% difference between the two ΔC_m vs J_{ss} slopes. The 100mm AFC consistently produced a slightly lower ΔC_m per J_{ss} than the 200mm AFC. This difference was due to the 200mm AFC entraining a consistently greater percentage of the propeller slipstream, even when placed at less optimal spanwise locations in relation to the propeller slipstream peak velocity. Additionally, the impact of edge effects—viscous drag due to sharp edges—are likely greater for the exit flow of the 100mm AFC than the 200mm AFC. Due to both the 100mm and 200mm AFC having the same edge designs, both actuators experience a fixed spanwise distance of lower performance due to this viscous drag effect. This results in a greater spanwise percentage of the shorter-span AFC actuator being impacted by the edge effect viscous drag, thus impairing the 100mm AFC with greater impact than the 200mm AFC.

If a Coanda actuator with different external profile or internal geometry were tested, the ΔC_m vs J_{ss} slope would also be different, but this linear relationship would still be expected. Therefore, using the approximate ΔC_m values can be computed using a linear relationship for TE AFC locations along a wing when the spanwise velocity profile is known at the chordwise AFC location. This relationship is not only useful for determining optimal TE AFC placement for maximum effectiveness, but it also allows for ΔC_m losses or gains to be characterized at multiple spanwise locations on a wing if ΔC_m at one location is measured since losses and gains scale according to J_{ss}. This is an

important finding as it enables approximate ΔC_m losses to be computed if an aircraft is designed such that TE AFC cannot be placed in the location of highest U_{ss}.

3.3 Varying AFC Geometry

This section of the results will present and explain the data collected from testing 14 Coanda AFC actuators with varying geometric configurations—with respect to their external profile shape and internal nozzle configuration—mounted at the center-span location (-0.52*R*:+0.52*R*) on the tabletop static test stand. All testing was performed at the same propeller conditions as in Section 3.2, including the constant 6000RPM setpoint. These results will be presented first as nondimensionalized lift force and pitching moment effect versus mass flow injection, then as nondimensionalized lift force versus AFC blowing cost per unit span, represented as momentum coefficient. This results section will include a discussion comparing values achieved by this study with existing literature detailing similar experiments with Coanda actuators.

3.3.1 Pitching Moment and Lift Force vs. Mass Flow

This section will present the data and describe trends attained from evaluating the 14 actuators of varying Coanda AFC geometry in terms of their performance in lift and pitching moment generation vs. mass flow rate injected to the AFC actuator. Load cell data in the next two sections are represented as nondimensional ΔC_L and ΔC_m–equations defined in section Data Analysis Methods—to quantify the change in lift and pitching moment from the nominal case of no blowing through the AFC actuator with the

propeller spinning at constant 6000RPM during all testing. Next in section 4.3.1.1, the continuous slot AFC ΔC_L and ΔC_m vs. mass flow data will be presented. Following in section 4.3.1.2, the discrete slot AFC ΔC_L and ΔC_m vs. mass flow data will be presented.

3.3.1.1 Continuous AFC Force and Moment Data

For the experiments involving 14 Coanda AFC actuators of varying configurations, the lift and pitching moment data were first characterized for the seven continuous slot actuators. The nondimensionalized lift and pitching moment results are displayed in Figure 26 and plotted vs. mass flow. The design in this study with the same profile as used by the varying spanwise AFC study—results explained in Section 3.2—with r=8mm and h=0.5mm was a separate 3D print and had one less internal diffusion grid and poorer exit slot uniformity performance—37% variation compared to 9% variation (Table 2 and Table 4).

The nonuniformity of the circular profile actuator in the present study (CC-R8-H0.5) produced a greater exit slot velocity on the side of the wing which experienced the descending propeller blade which aligned with the location of maximum propeller slipstream. This resulted in increased flow entrainment by the circular actuator in the present study (ID-CC-R8-H0.5) and resulted in ΔC_L=0.90, which is a 9% increase over the ΔC_L=0.82 achieved by the 200mm actuator in the experiments which involved varying spanwise AFC location. The difference in ΔC_m values compared to the varying spanwise AFC location study was within the instrument uncertainty, so it is inconclusive

whether this change in pitching moment between the two testing campaigns was due to instrumentation or physical mechanisms.

In the varying AFC configuration component of this study, the maximum ΔC_L from center-span, continuous AFC tests was 0.90, and the maximum ΔC_m was 0.44, both achieved by the half-circular design with r=8mm and displayed in Figure 26. These values are 0.08 and 0.06 greater—9% increase in lift and 15% increase in pitching moment—than the respective values obtained in the varying spanwise AFC experiments. Although this design was most effective for improving lift and pitching moment, it cannot be used for dual-slot actuation. The design that achieved an equal ΔC_L of 0.90 and a slightly lower ΔC_m=0.38 was the baseline with a radius of 8mm and slot height of 0.5mm (ID CC-R8-H0.5).

Also achieving a ΔC_m=0.38 was the actuator which had the smallest radius r=4mm (ID CC-R4-H0.5) which resulted in the longest moment arm when extended along the NACA 0012 profile, giving this design an inherent ΔC_m advantage. The moment arm of CH-R8-H0.5 was 36mm longer than that of the baseline CC-R8-H0.5. With a Coanda surface r=4mm, CC-R4-H0.5 was not as effective at producing lift as the baseline CC-R8-H0.5 actuator due to the baseline design having a smaller and more optimized h/r. The baseline CC-R8-H0.5 actuator is the most optimized design with the capability to be altered for dual-slot actuation by opening the sealed side of the actuator. From these data, it can be concluded that the elliptic and bi-convex actuator profiles were not as effective in producing lift and pitching moment benefits as the baseline circular

Coanda surface, as these profiles were out-performed by the circular and half circular profiles for both lift and pitching moment.

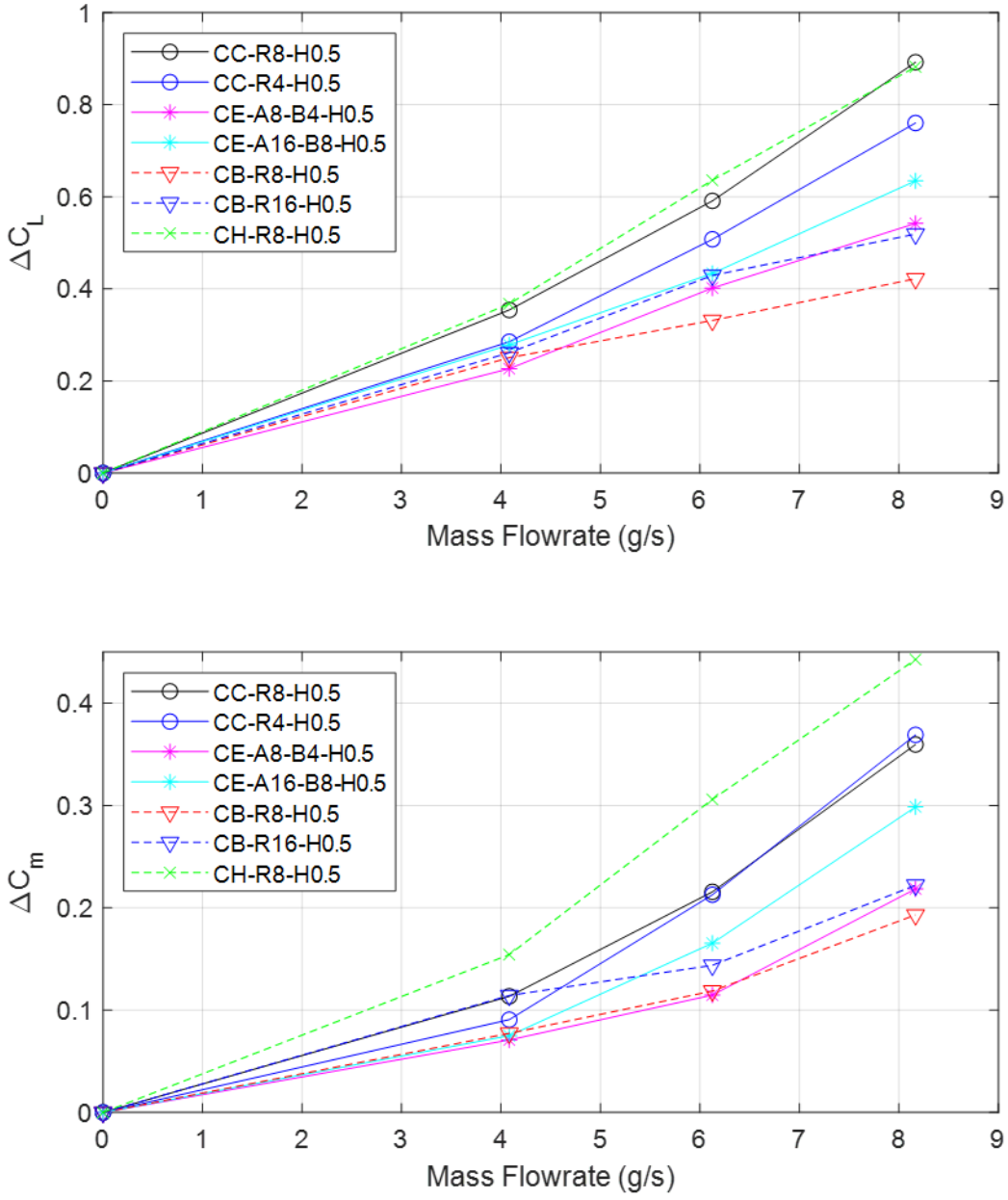

Figure 26: ΔC_L and ΔC_m vs. mass flow for continuous slot Coanda actuators with varying profile.

3.3.1.2 Discrete AFC Force and Moment Data

Next, the discrete slot and fluidic oscillator (FO) AFC configurations were tested and evaluated in terms of the forces and moments each produced on the static test stand set up with the propeller running. The nondimensional lift and pitching moment data from these actuator designs are displayed in Figure 27 and plotted against increasing mass flow injection setpoints. Also included in this figure are the results from the baseline continuous slot actuator (ID CC-R8- H0.5), to display the results from all actuators with the circular, r=8mm external Coanda profile in the same plot. This provides a direct comparison between the continuous slot, discrete jet, and fluidic oscillator AFC designs.

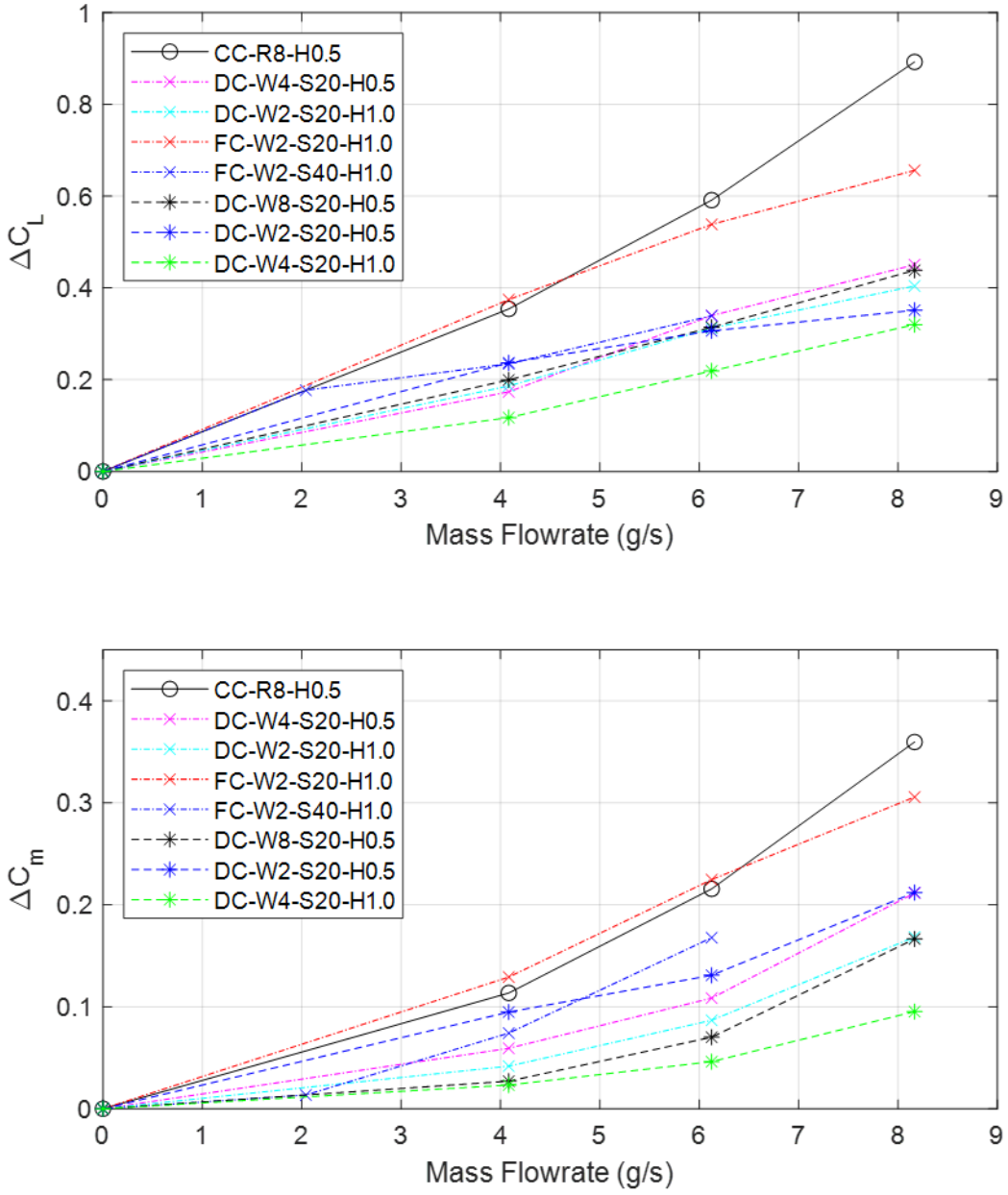

Figure 27: ΔC_L and ΔC_m vs. mass flow for actuators with circular profile and r=8mm.

From these data, it can be concluded that the baseline continuous slot actuator (ID CC-R8-H0.5) is the most optimal design for lift and pitching moment performance at high mass flow injections. However, the ΔC_L and ΔC_m achieved by this baseline continuous design—detailed in the explanation of Figure 26—were closely matched or out-performed by the discrete slot actuator with ten FOs (ID FC-W2-S20-H1.0) at low mass flow injections. (Note that the FOs in this actuator were functioning at 90% sweeping jet effectiveness due to manufacturing imperfections.) At the first mass flow setpoint of 4g/s, the FO outperformed the baseline actuator in both lift and pitching moment by margins of 4% and 15% respectively. At the second setpoint of 6g/s, the FO continued to outperform the continuous baseline in pitching moment performance by a margin of 4% but was outperformed by the baseline design by a margin of 10% for lift. At the final mass flow injection setpoint of 8g/s, the baseline continuous design outperformed the FO design by margins of 33% and 18% for lift and pitching moment, respectively. This indicates that FO performance may be degraded at higher mass flow setpoints. During testing, it was qualitatively observed that large back pressures caused the FO exit flow to push straighter through the exit without wrapping around the external Coanda surface effectively (Figure 15). Exit slot uniformity degradation at higher mass flow injections could also cause decreased performance.

The discrete jet and FO actuators consistently required 25-50% greater back pressures to operate than the continuous, since they pushed equal mass flow through smaller exit areas. All continuous actuators had an exit slot area of $100mm^2$, whereas the FOs in this study had exit areas of $10mm^2$ (ID FC-W2-S40-H1.0) and $20mm^2$ (ID FCW2-

S20-H1.0) which are only 10% and 20% of the exit area of the continuous slot actuator, respectively. The FOs produced significant geometric barriers, and the mass flow controller required over 40 PSID to operate these actuators at the second setpoint of 6g/s. The actuator design with five FOs (ID FC-W2-S40-H1.0) could not reach the final mass flow setpoint of 8g/s due to this high back pressure requirement for FOs combined with having the smallest exit area of $10mm^2$. The baseline continuous slot actuator remains most feasible for in-flight application due to its consistent, continually improving performance and 25-50% lower back pressure requirements compared to the FO actuators—40 PSI at 8g/s rather than 40 PSID at 6g/s. This indicates that FO designs manufactured and tested in this study slot spacing distances that were too large to require large back pressures and even have back pressure as a limitation for testing. If FO actuators of the same span were designed with reduced slot spacing, the exit slot area would increase, and the back pressure requirements would be reduced. This would likely cause the sweeping jets to improve in performance consistency, resulting in the FO designs to be less limited and potentially more effective than the continuous slot AFC for a greater range of mass flow injections.

The goal with testing the discrete slot actuators was to achieve improved exit slot uniformity and similar or improved force and moment outputs over the continuous slot AFC designs. Although the discrete jet designs performed well overall in terms of their exit slot velocity uniformity (Table 5), the non-sweeping discrete jet actuators demonstrated significantly degraded performance compared to the ten FO and continuous baseline designs, averaging 50-80% lower ΔC_L and ΔC_m values at all mass flow injection

setpoints tested. This deficient performance could be due to several factors, one being the difference in slot height between discrete jet actuator designs compared to continuous slot actuator designs. Wilde in 2009 explained that reducing *h/r* for Coanda actuators leads to improved flow attachment and redirection along the curved surface, ultimately yielding improved force and moment generation from Coanda actuators [10]. This was supplemented by Henry and Williams in 2018, who showed that improved attachment and force output has been demonstrated for *h/r* values as low as 0.05 [25].

All discrete jet actuators had a slot height *h*=1.0mm to maintain a minimum of $10mm^2$ exit area while testing various slot spacings and configurations. This minimum exit area was set in the design stage to prevent equipment back pressure limitations and maintain the same mass flow setpoints for all actuators during testing. This resulted in *h/r*=0.12 for all discrete actuators (including FOs), which is two times greater in magnitude than that of the continuous slot AFC actuators (*h/r*=0.062). This greater exit slot height and *h/r* was a probable cause of the degraded flow wrapping around the Coanda surface. The spacing between discrete jets is another parameter that was not optimized in this study due to consistently poor performance of non-sweeping discrete jets and needs to be further evaluated. To characterize discrete slot actuators in more of a direct comparison, the exit slot height should be reduced to *h*=0.5mm, and more spanwise slots with decreased slot spacing should be added to maintain the minimum $10mm^2$ exit slot area.

3.3.2 Momentum Coefficient Per-Span Cost Analysis

This section will present the data and describe trends attained from evaluating the 14 actuators of varying Coanda AFC geometry in terms of their performance in lift and pitching moment generation vs. momentum coefficient, C_μ. Load cell data in the next two sections are represented as nondimensional ΔC_L and ΔC_m–equations defined in section Data Analysis Methods—to quantify the change in lift and pitching moment from the nominal case of no blowing through the AFC actuator with the propeller spinning at constant 6000RPM during all testing. Next in section 4.3.2.1, the continuous slot AFC ΔC_L and ΔC_m vs. C_μ data will be presented. Following in section 4.3.2.2, the discrete slot AFC ΔC_L and ΔC_m vs. C_μ data will be presented.

3.3.2.1 Continuous AFC Momentum Coefficient Analysis

To characterize the seven continuous AFC actuators used in this study, the lift coefficient versus momentum coefficient curve was computed and is displayed in Figure 28. The data in this Figure represent the same ΔC_L trend as the previous figure but characterizes the cost per unit span associated with each ΔC_L in a manner comparable to related Coanda AFC studies in recent literature. Since all continuous slot actuators had the same geometric exit slot characteristics—slot height of 0.5mm and span of 200mm (1.05R)—the C_μ for all seven actuators at each mass flow setpoint was equal. The maximum C_μ for all actuators was 0.18 (18%), with the baseline design and the half-circular design both achieving the maximum ΔC_L=0.90.

The least optimal design was the bi-convex profile with a radius of 8mm. The deficient performance of bi-convex profile designs in Figure 26 was due to the trailing edge surface angled at 45° to the chord (C, Figure 16) which limited the turning angle of the flow and redirection of momentum normal to the chord. This was qualitatively observed by hand feeling the flow during testing. Similar qualitative observations were made for the elliptical designs and their flow wrapping, which was similarly impeded by the lack of immediate surface curvature compared to circular profile designs. This finding agrees with a previous study by Alexander et al. which reviewed elliptical Coanda surfaces with slot actuator along the trailing edge of a wing [32]. They compared elliptical trailing edge designs with a constant minor axis size (B, Figure 16) and greater varying major axis lengths (A, Figure 16).

At the freestream Mach number of 0.3 and 6° angle of attack, Alexander et al. found that the Coanda actuator design with the shortest major axis length, which was more circular, had the greatest increases in lift and pitching moment compared to designs with longer major axis lengths of their elliptical profiles [32]. This more circular design achieved maximum ΔC_L=0.7 and maximum ΔC_m=0.5 at C_μ=0.04, compared to the design with the longest major axis which achieved maximum ΔC_L=0.5 and maximum ΔC_m=0.4 at C_μ=0.1 [32]. The actuator with the shortest major axis achieved a maximum dC_L/C_μ=33, whereas the actuator with the longest major axis achieved a maximum dC_L/C_μ=13, both at C_μ=0.01 [32]. The lowest momentum coefficient tested for the present study was C_μ=0.04, where the elliptical actuators, CE-A8-B4-H0.5 and CE-A16-B8-H0.5, achieved dC_L/C_μ=7 and dC_L/C_μ=6, respectively. At the C_μ=0.04 setpoint, the

dC_L/C_μ=15 for the shortest major axis design and dC_L/C_μ=10 for the longest major axis design evaluated by Alexander et al. [32]. Considering the tests were performed by Alexander et al. in freestream conditions with greater momentum supplied and a greater angle of attack, improved lift performance—even by a factor of two—is expected.

Having the greatest angular curvature immediately following the exit slot—also the smallest *h/r*—causes the greatest and most immediate pressure drop experienced by airflow, further pressing on the fluid as it wraps around the Coanda surface and increasing force generation. However, these data indicate that there is a limit to this curvature as smaller radiuses provide less area over which the low pressure can act and can lead to earlier separation of the flow, lessening the Coanda effect. This is shown by comparing the CC-R8-H0.5 lift coefficient performance with the CC-R4-H0.5 actuator. Both actuators have a slot height of 0.5mm, but the actuator with *r*=8mm (*h/r*=0.062) outperforms the actuators with *r*=4mm (*h/r*=0.12) by 17%. Thus, the circular Coanda actuators with *h/r*=0.062 most effectively wrapped AFC injected flow around the Coanda surface and entrained flow provided by the propeller slipstream.

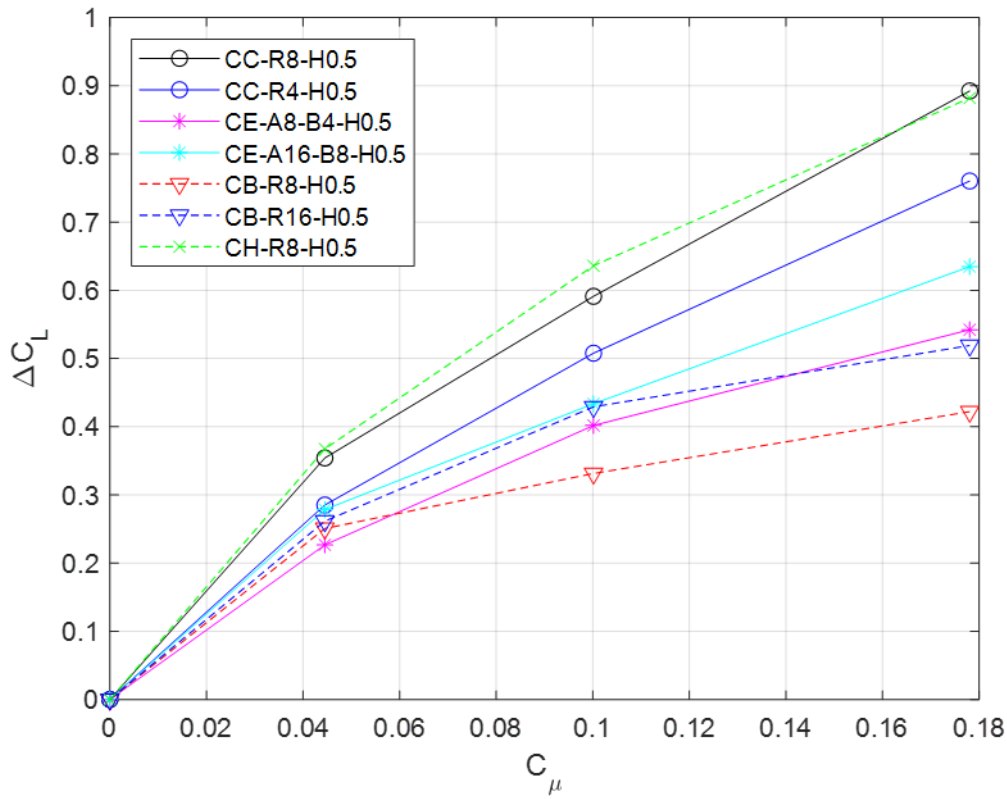

Figure 28: ΔC_L vs. C_μ for continuous slot Coanda actuators of varying profile.

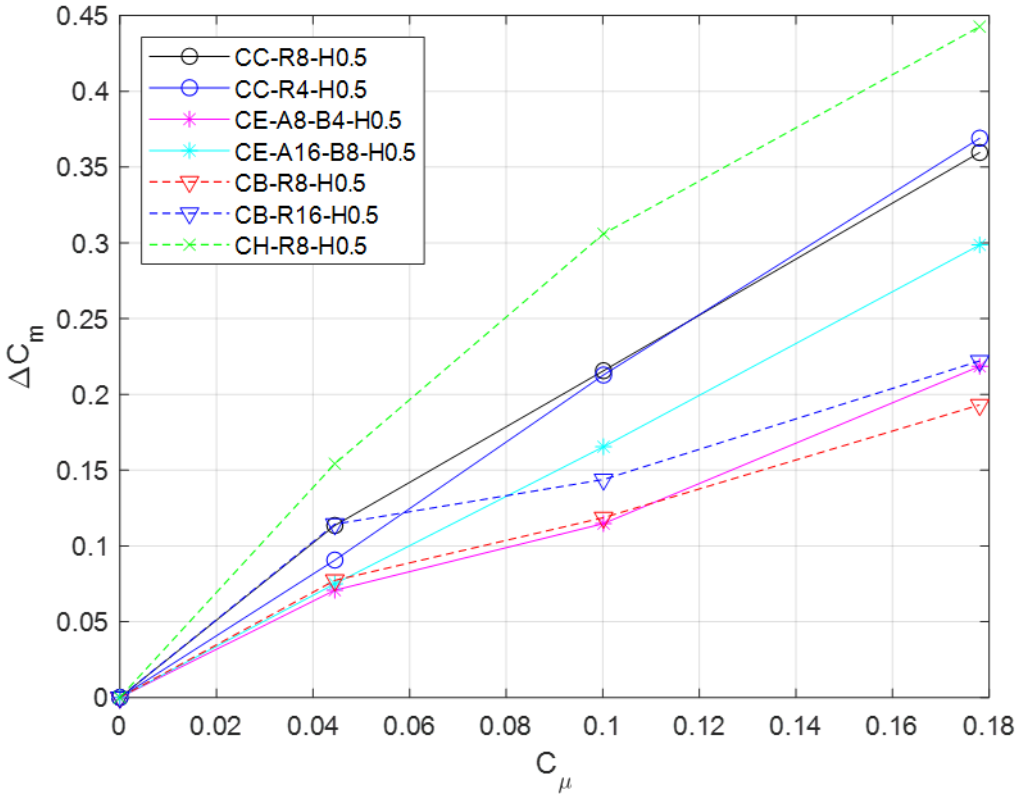

Figure 29: ΔC_m vs. C_μ for continuous slot Coanda actuators with varying profile.

When evaluated in terms of dC_L/dC_μ as in Figure 28, the baseline circular (ID CC-R8-H0.5) and half-circular profile (ID CH-R8-H0.5) Coanda actuators in this study yielded the most optimal performance. For this actuator, the highest 8g/s mass flow setpoint corresponded to a C_μ=0.18 where both actuators achieved a ΔC_L=0.90. and a resulting dC_L/dC_μ=5.0. Also, for this FO actuator, the lowest mass flow setpoint corresponded to a C_μ=0.04 where these actuators achieved a ΔC_L=0.36 and a resulting dC_L/dC_μ=8.8.

However, as shown in Figure 29, the half-circular r=8mm Coanda actuator (ID CH-R8-H0.5) yielded optimal performance when evaluated in terms of dC_m/dC_μ. For this actuator, the highest 8g/s mass flow setpoint corresponded to a C_μ=0.018 where this actuator achieved a ΔC_m=0.44 and a resulting dC_m/dC_μ=2.4. The FO actuator also achieved ΔC_m=0.16 at the lowest mass flow setpoint corresponded to a C_μ=0.04 where this actuator achieved a resulting dC_m/dC_μ=3.9. The baseline circular r=8mm actuator (ID CC-R8-H0.5) was the second-best overall for dC_m/dC_μ performance, achieving ΔC_m=0.36 and dC_m/dC_μ=2.0 at the highest mass flow setpoint of 8g/s and ΔC_m=0.12 and dC_m/dC_μ=2.9 at the lowest mass flow setpoint of 4g/s. as stated, the improved pitching moment generation by CH-R8-H0.5 over that of CC-R8-H0.5 can be explained by the difference in moment arm lengths between the actuators which was necessary to maintain the NACA 0012 airfoil profile with varying TE AFC shapes.

3.3.2.2 Discrete AFC Momentum Coefficient Analysis

To characterize the performance and cost per unit span of continuous and discrete slot designs for AFC actuators, the ΔC_L vs. C_μ curve for all actuators with radius of 8mm is displayed in Figure 30. This external profile was used to evaluate discrete AFC performance due to its optimal continuous slot performance compared to other profiles tested in this study combined with its adaptability for dual-slot actuation which is not possible for the half-circular design. Since the exit slot area was not equal for these designs (see Table 5), the per-span costs associated with each, evaluated as C_μ, varied with the same mass flow injection setpoints. Note that the reference area for momentum

coefficient was exit slot area—not throat area—for the FO designs. Based on these curves, the actuator with ten FOs (ID FC-W2-S20- H1.0) achieves greater ΔC_L with lower per-span cost compared to the baseline continuous design (ID CC-R8-H0.5). However, the continuous actuator achieved an overall greater ΔC_L without the same back pressure limitations experienced by the discrete jet and FO actuators. Therefore, the baseline continuous actuator remains most optimal for in-flight applications compared to the other geometric designs tested in this study. Note that the internal uniformity grids were designed for the continuous slot actuators to ensure exit slot uniformity, and this design was carried over to the discrete slot actuators. It is possible the elevated back pressures experienced by discrete slot and FO actuators were caused in part by the internal grids, and more optimization work must be done to determine if back pressure can be reduced while maintaining exit slot uniformity for discrete slot actuators.

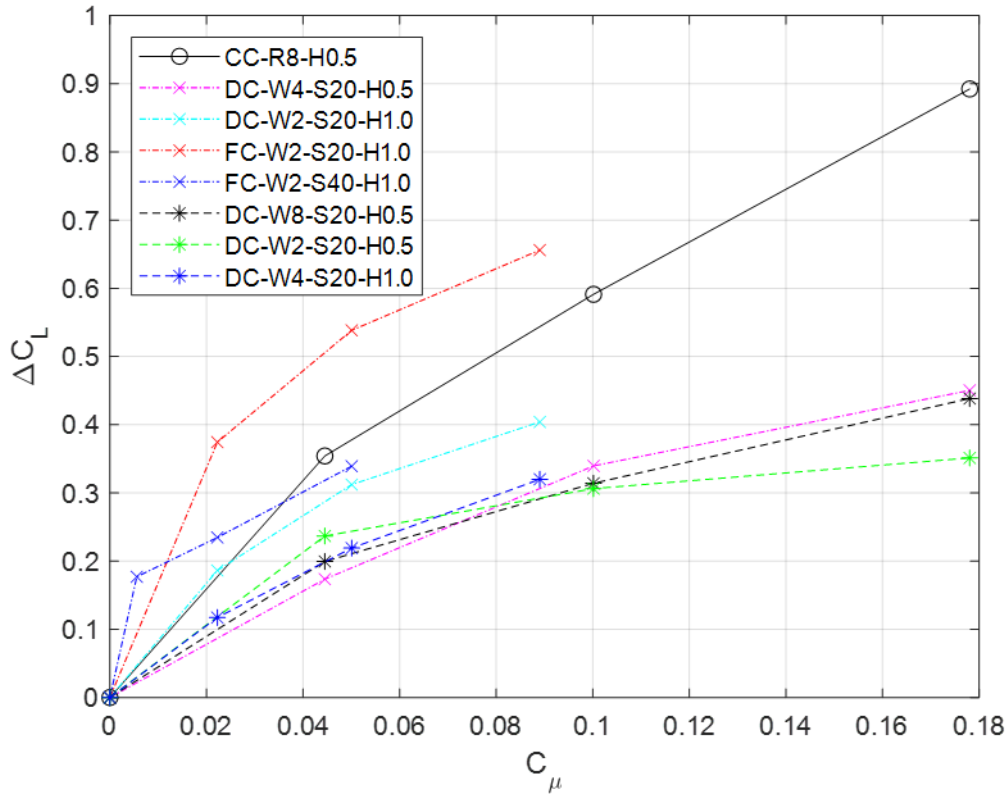

Figure 30: ΔC_L vs. C_μ for actuators with circular profile and r=8mm.

When evaluated in terms of dC_L/dC_μ the Coanda actuator with ten FOs in this study (ID FC-W2-S20-H1.0) yielded the most optimal performance. For this actuator, the highest 8g/s mass flow setpoint corresponded to a C_μ=0.09 where this actuator achieved a ΔC_L=0.65 and a resulting dC_L/dC_μ=7.2. Also, for this FO actuator, the lowest mass flow setpoint corresponded to a C_μ=0.02 where this actuator achieved a ΔC_L=0.38 and a resulting dC_L/dC_μ=19. Although the FO actuator was unable to generate lift forces as effectively as the baseline circular Coanda actuator (ID CC-R8-H0.5) per unit of mass

flow injection, its performance was most optimal when analyzed in terms of lift generation per momentum coefficient.

Similarly, as shown in Figure 31, Coanda the actuator with ten FOs in this study (ID FC-W2-S20-H1.0) yielded optimal performance when evaluated in terms of dC_m/dC_μ. For this FO actuator, the highest 8g/s mass flow setpoint corresponded to a C_μ=0.09 where this actuator achieved a ΔC_m=0.31 and a resulting dC_m/dC_μ=3.4. The FO actuator also achieved ΔC_m=0.13 at the lowest mass flow setpoint corresponded to a C_μ=0.02 where this actuator achieved a. and a resulting dC_m/dC_μ=6.5. Although the FO actuator was unable to generate pitching moment as effectively as the baseline circular Coanda actuator (ID CC-R8-H0.5), its performance was most optimal in terms of pitching moment generation per momentum coefficient.

Based on the trends presented in Figure 30 and Figure 31, if lower mass flow injections were tested the dC_L/dC_μ and dC_m/dC_μ may be greater than the values presented in the previous paragraphs. However, the focus of this study was on higher blowing rates since the primary goal was to maximize force and moment generation with TE Coanda AFC so mass flow injection setpoints lower than 2g/s for the 200mm Coanda AFC actuators were not evaluated.

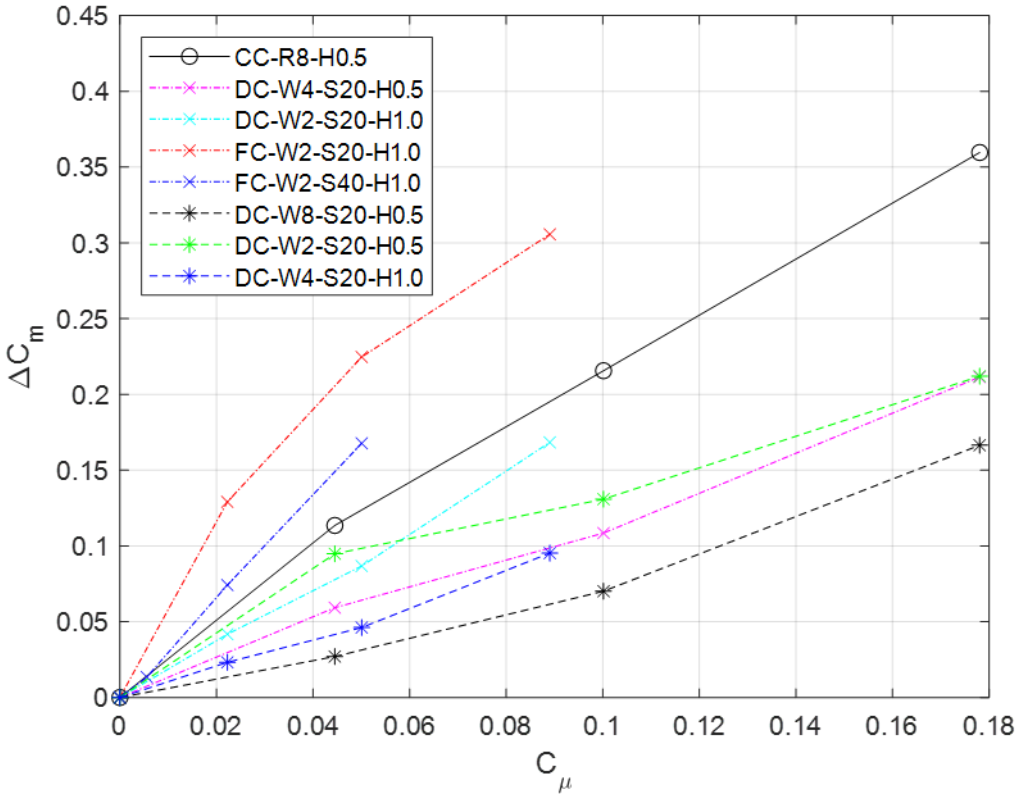

Figure 31: ΔC_m vs. C_μ for actuators with circular profile and r=8mm.

3.3.3 Comparison to Existing Designs

The ΔC_L vs C_μ curve for the continuous slot actuators follows the same trend and relative values as the work of other aerodynamicists who have developed and tested Coanda AFC actuators in recent years. Figure 32 shows the results from the circular Coanda actuator in this varying geometry investigation compared to similar designs from other researchers.

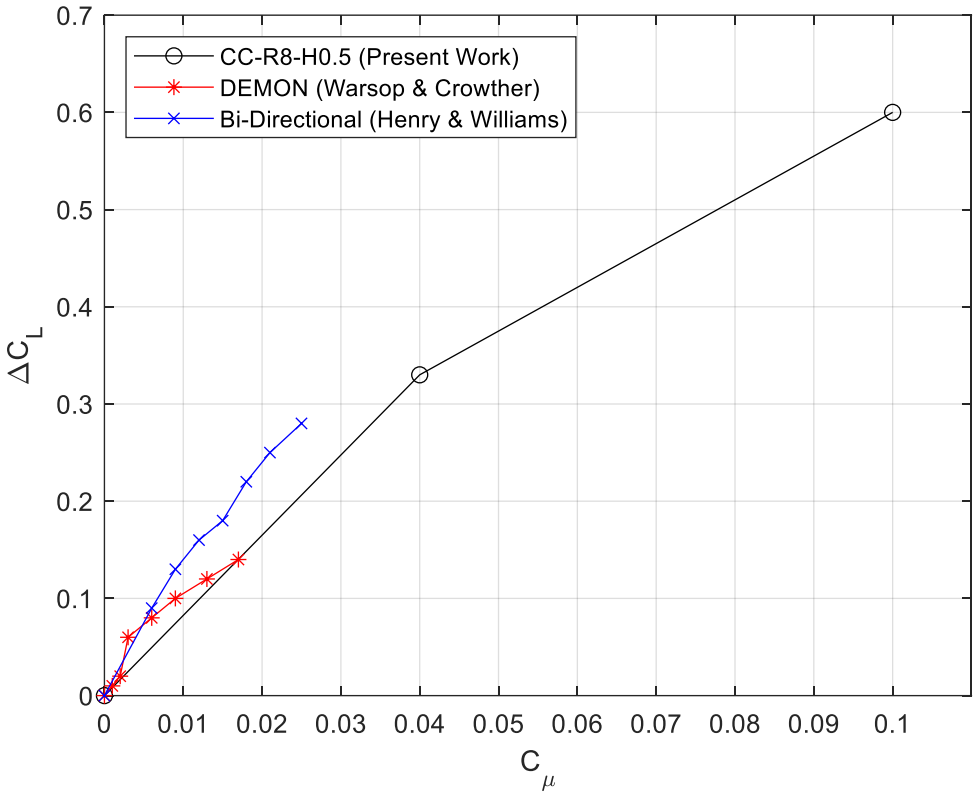

Figure 32: Plot displaying the ΔC_L vs C_μ curve from CC-R8-H0.5 in the present work up to C_μ=0.1 compared to similar Coanda actuator designs from Warsop & Crowther [22] and Henry & Williams [25].

Warsop and Crowther in 2018 documented results from a Coanda actuator on the DEMON aircraft with a circular profile and h/r=0.067 with h=0.2mm and r=3mm. This design achieved a maximum ΔC_L=0.14 with a momentum coefficient of C_μ=0.017, yielding a dC_L/dC_μ=8 at this maximum setpoint and dC_L/dC_μ>30 at lower blowing rates with a freestream velocity of 20m/s [6]. The dC_L/dC_μ achieved by the circular r=8mm continuous AFC Coanda actuator in this study was 5.0 at the point maximum injection flow—only 60% of the dC_L/dC_μ achieved by Warsop and Crowther. The maximum

dC_L/dC_μ for this actuator was 8.8—less than 30% of the maximum achieved by Warsop and Crowther—which occurred at the lowest point of injection flow tested in this study. If lower mass flow injections were tested, the dC_L/dC_μ may be even greater.

Although the dC_L/dC_μ was lower for the circular Coanda actuator in the present study, the maximum ΔC_L was four times greater than that of the DEMON aircraft AFC. The Coanda surface in this study used a similar h/r=0.062 but h and r were scaled up by a factor of 2.67, and this scaling difference combined with the difference in velocity source were likely causes for improved performance over the Coanda actuators in this study. Comparison between the DEMON aircraft performance indicates there is room for improvement in terms of dC_L/dC_μ for this study's Coanda surface design, but it performs well in terms of force generation.

Henry and Williams tested a Coanda actuator with h/r=0.05 which achieved a lift coefficient of 0.3 at a momentum coefficient of 0.025, yielding a dC_L/dC_μ=11 at this maximum blowing setpoint and dC_L/dC_μ=15 at lower blowing rates [25]. The Coanda actuators in the Henry and Williams' study were sweeping jets and testing was conducted in a wind tunnel with freestream velocities of up to 28m/s. Although a direct comparison cannot be made to the present study, it is useful to understand that with a similar h/r=0.062, the Coanda AFC actuator in the present study yielded consistently lower dC_L/dC_μ values, indicating improvements are necessary with blowing efficiency.

Furthermore, the per-span cost performance of the FO Coanda actuator aligns more closely with dC_L/dC_μ values documented by aerodynamicists in recently published literature. Warsop and Crowther documented a dC_L/dC_μ=8 with maximum mass flow

injection and maximum dC_L/dC_μ>30 at lower blowing rates for the DEMON aircraft which used a circular Coanda surface profile with h/r=0.067 and continuous slot blowing [6]. This optimal FO design (ID CC-R8-H0.5) is also comparable to Henry and Williams' sweeping jet Coanda actuator with h/r=0.05 which achieved a dC_L/dC_μ=11 at the maximum blowing setpoint and dC_L/dC_μ=15 at lower blowing rates [25]. The highest performing FO design in the present study yielded dC_L/dC_μ values which were of similar magnitude to published literature on FO and circular Coanda AFC performance.

Chapter 4. Conclusions and Future Work

4.1 Conclusions

This section will summarize and describe the main takeaways from the experiments which compose this collective study of TE Coanda AFC actuators and factors which impact their effectiveness for the case of hover flight with momentum supplied by an upstream propeller. Next, section 5.1.1 will present the conclusions from varying AFC spanwise location experiments, and conclusions for varying AFC geometry will be presented subsequently in section 5.1.2.

4.1.1 Varying AFC Spanwise Location Conclusions

The focus of this study was to determine the optimal placement of Coanda actuators as trailing edge control effectors in the hover flight case with an upstream propeller. For this testing, momentum was provided only by the rotor, and testing was performed on a static test stand with a wing configured with AFC Coanda actuators at varying locations along the trailing edge to study which locations provide the greatest and least optimal performance, evaluated in terms of pitching moment and lift coefficients. Based on initial velocity profile testing and a literature review of propeller slipstream over a downstream wing, it was theorized that the most beneficial location of AFC actuators was skewed towards the downwash side of the wing. The findings from the

pitching moment evaluation supported this theory clearly for the AFC spanning 100mm (0.52R). The AFC actuator spanning 200mm (1.05R) was less sensitive but still showed slight improvement when placed with 60% of its span on the downwash side.

The second goal of this work was to achieve a direct comparison between Coanda AFC actuators and a traditional trailing-edge control surface deflection. To accomplish this, testing was conducted to evaluate the performance of a deflected control surface of NACA 0012 profile was fabricated to be equal in span to the 200mm (1.05R) Coanda actuator section. This traditional control surface section was tested at center span of the wing with different angular deflections to determine how AFC blowing rates compare with control surface deflections in terms of control authority and lift generation. It was found that at the highest AFC blowing setpoint, the Coanda actuator produced 90% of both lift and pitching moment produced by the deflected surface.

Finally, analysis was performed to yield an approximate linear relationship between pitching moment achieved by each TE Coanda AFC actuator and the TE momentum flux over the wing at the location of AFC placement. This relationship holds true for varying AFC actuator lengths and demonstrates that control authority of AFC is directly proportional to local momentum flux. With knowledge of the velocity profile along a wing, TE AFC placement can be optimized. With additional knowledge of pitching moment from TE AFC at one spanwise location, control authority can be approximated for other locations along the span.

4.1.2 Varying AFC Geometry Conclusions

In conclusion, an experimental static test stand setup was constructed to compare various trailing edge Coanda AFC actuator nozzle types and geometric configurations in terms of pitch control performance and lift production. The source of airflow over the wing was a forward-mounted propeller emulating a vertical takeoff aircraft in hover. All AFC actuators tested were of equal span and measured 105% of the propeller radius (1.05R). Varying mass flow rates were supplied to the AFC actuators while the upstream propeller was held at a constant RPM setpoint.

The results from varying AFC geometric configuration show that the optimal trailing-edge Coanda actuator design was the continuous slot design with a circular profile and radius of 8mm and slot height of 0.5mm (h/r=0.062). However, the actuator which followed the same circular h/r=0.062 profile and had ten spanwise fluidic oscillators in place of the continuous slot produced optimal performance at lower mass flow rates but required back pressures which were 25-50% greater than the continuous slot designs. The associated flow requirement costs were also explored and used to determine the momentum coefficient to characterize the cost per unit span of each configuration.

4.2 Future Work Recommendations

This section will describe the avenues of research pursuit recommended based on the findings in this thesis. Next, section 5.2.1 will describe the future work recommended based on findings from the experiments which characterized the effect of varying AFC

spanwise location in the propeller slipstream. Finally, section 5.2.2 will describe recommended future work based on findings from the varying AFC configuration experiments.

4.2.1 Varying AFC Spanwise Location Future Work

One research avenue recommended to build on the experiments in which TE Coanda AFC spanwise location was varied within a propeller slipstream is to alter the wing sweep. The straight wing with a sweep of 0° design may not be ideal for the final tail-sitting VTOL UAV vehicle with the objective of full AFC control. Experiments should be conducted which test various spanwise AFC locations on swept wings with varying degrees of sweep. This testing would provide information on how wing sweep affects the propeller slipstream skew and resultantly how wing sweep impacts TE Coanda AFC flow entrainment, leading to force and moment generation.

The effect of TE Coanda AFC placement should also be evaluated with freestream flow. This testing can be conducted with a similar propeller-wing setup as the present work, but inside a wind tunnel or with an alternate uniform momentum source to inform on the effect of TE Coanda AFC in cruise flight.

4.2.2 Varying AFC Geometry Future Work

One avenue of future research pursuit recommended based on the findings from the varying AFC geometry experiments is optimizing the FO performance for TE Coanda AFC implementation. The FO oscillation performance was 80-90% for the Coanda AFC

actuators in this study, indicating room for improvement in the manufacturing process. Furthermore, the FO sizing and spacing should be revisited in future work to investigate why the actuator with 10 FOs yielded greatest performance at low blowing rates but was outperformed by the baseline Coanda AFC design at higher blowing rates. Another avenue of research which may be integrated into the FO-Coanda combination is the curved FO device, which was recently studied by Spens et al. with the intended application of leading-edge FO blowing, but curved FOs may be implemented onto the Coanda surface itself to improve flow attachment [12].

Another avenue of interest regarding Coanda AFC configuration is to evaluate variations in actuator slot height and radius combinations. This research avenue is recommended to focus on characterizing the impact of the *h/r* parameter for lift force and pitching moment generation versus mass flow. This *h/r* variation is of particular interest because literature has found that decreasing *h/r* increases Coanda jet flow wrapping performance—which results in increased force and moment generated by AFC to benefit the overall system.

A final future research route for the present work is implementing a multidirectional Coanda actuator, like the IIT group has done for their AFC flight vehicle [25]. The effect of a multidirectional 200mm Coanda AFC actuator should be compared to the effect of two adjacent unidirectional 100mm actuators blowing in opposite directions—and located at the optimal M_z location respective to each blowing direction—to evaluate the benefits and costs of each configuration in the presence of the skewed propeller slipstream flow. This

will inform how to capitalize on the control authority generated by AFC for the VTOL flight vehicle configuration most effectively.

References

[1] Defense Science Board, "Defense Sceince Board Task Force on Future Need for VTOL/STOL Aircraft," Office of the Under Secretary of Defense, Washington, D.C., 2007.

[2] J. R. Hoehn, K. M. Sayler and M. E. DeVine, "Unmanned Aircraft Systems: Roles, Missions, and Future Concepts," Congressional Research Service, 2022.

[3] J. D. J. Anderson, Introduction to Flight, Eighth Edition, New York, NY: McGraw-Hill Education, 2016, pp. 294-300.

[4] R. G. Simpson, N. A. Ahmed and R. D. Archer, "Improvement of a Wing's Aerodynamic Efficiency Using Coanda Tip Jets," *J. Aircraft: Engineering Notes,* vol. 37, no. 1, pp. 183-184, 1999.

[5] V. K. Reddy and R. Woszidlo, "Scaling of the Momentum Coefficient from Fluidic Oscillators at Different Ambient and Supply Conditions," in *AIAA SciTech Forum*, National Harbor, MD, 2023.

[6] C. Warsop and W. J. Crowther, "Fluidic Flow Control Effectors for Flight Control," *AIAA Journal,* vol. 56, no. 10, pp. 3808-3824, 2018.

[7] M. DeSalvo, E. Whalen and A. Glezer, "High-Lift Performance Enhancement Using Active Flow Control," *AIAA Journal,* vol. 58, no. 10, pp. 4228-4242, 2020.

[8] R. Drenovsky, "Henri Coanda Papers [Stine]," [Online]. Available: https://sova.si.edu/record/NASM.XXXX.0170?s=0&n=10&t=K&q=*&i=0.

[9] NASA Spaceflight Forum, "Flying saucers R&D - The Coanda effect," [Online]. Available: https://forum.nasaspaceflight.com/index.php?action=dlattach;topic=41732.0;attach=1404774;sess=0. [Accessed 3 January 2024].

[10] P. A. I. Wilde, "The Application of Circulation Control for Three Axis Control of a Tailless Aircraft," The University of Manchester, Manchester, England, 2009.

[11] T. Srinivas, B. Vasudevan and A. Prabhu, "Perfromance of Fluidically Controlled Oscillating Jet," in *IUTAM Symposium,* Bangalore, India, 1988.

[12] A. Spens, P. J. Brandt and J. P. Bons, "Characterization of Out-of-Plane Curved Fluidic Oscillators," *AIAA Journal,* 2024.

[13] R. Woszidlo and I. Wygnanski, "Parameters Governing Separation Control with Sweeping Jet Actuators," in *29th AIAA Applied Aerodynamics Conference*, Honolulu, Hawaii, 2011.

[14] M. Koklu, "Effects of Sweeping Jet Actuator Parameters on Flow Separation Control," *AIAA Journal*, vol. 56, no. 1, pp. 100-110, January 2018.

[15] B. Vukasinovik, R. B. Funk and A. Glezer, "Circulation Control using Arrays of Discrete Fluidic Actuator Jets," in *AIAA SciTech Forum*, National Harbor, MD, 2023.

[16] P. M. J. Lovel, "Flight Tests of a 0.13-Scale Model of the Convair XFY-1 Vertically Rising Airplane With The Lower Vertical Tail Removed," Langley Aeronautical Laboratory, Langley Field, VA, 1954.

[17] R. H. Kirby, "Stability and Control Flight Tests of a Vertically Rising Airplane Model Similar to the Lockheed XFV-1 Airplane," Langley Aeronautical Laboratory, Langley Field, VA, 1954.

[18] P. M. J. Lovell, R. H. Kirby and C. C. J. Smith, "Flight Investigation of the Stability and Control Characteristics of a 0.13-Scale Model of the Convair XFY-1 Vertically Rising Airplane During Constant-Altitude Transitions," Langley Aeronautical Laboratory, Langley Field, VA, 1963.

[19] R. O'Rourke, "Unmanned Vehicles for U.S. Naval Forces: Background and Issues for Congress," 25 October 2006. [Online]. Available: https://www.history.navy.mil/research/library/online-reading-room/title-list-alphabetically/u/unmanned-vehicles-for-us-naval-forces-background-and-issues-for-congress.html. [Accessed 24 January 2024].

[20] M. W. Kelly and L. H. Smaus, "Flight Characteristics of a 1/4 Scale Model of the XFV-1 Airplane," Ames Aeronautical Laboratory, Mott Field, CA, 1952.

[21] A. Yarf-Abasi and J. Fielding, "DESIGN INTEGRATION OF THE ECLIPSE AND DEMON DEMONSTRATOR UAVs," in *AIAA Aviation Technology, Integration and Operations Conference*, Belfast, North Ireland, 2007.

[22] C. Warsop, W. J. Crowther and T. Shearwood, "NATO AVT-239: Flight Demonstration of Fluidic Flight Controls on the MAGMA Subscale Demonstrator Aircraft," in *AIAA SciTech Forum*, San Diego, CA, 2019.

[23] "Illinois Tech Professor Demonstrates Novel Control Method in Aircraft with No Tail," Illinois Institute of Technology, 7 February 2023. [Online]. Available: https://www.iit.edu/news/illinois-tech-professor-demonstrates-novel-control-method-aircraft-no-tail. [Accessed 26 January 2024].

[24] D. Greenblatt and D. Williams, "Flow Control for Unmanned Aerial Vehicles," *Annual Review of Fluid Mechanics*, vol. 54, no. 412, pp. 383-, 2022.

[25] J. Henry and D. R. Williams, "Performance Analysis of High-Frequency Oscillating Circulation," in *AIAA SciTech Forum*, National Harbor, MD, 2023.

[26] T. R. Shearwood, M. R. A. Nabawy, W. J. Crowther, R. P. Geraets, M. K. Quinn, S. Weigert, C. Warsop, M. Forester and L. Axani, "DARPA CRANE – A toolset for the design of compact fluidic distribution systems for flow control applications: Part 1 - Model development and system optimisation," in *AIAA SciTech Forum*, National Harbor, MD, 2023.

[27] T. R. Shearwood, R. A. N. Mostafa, W. J. Crowther, R. P. Geraets, M. K. Quinn, S. Weigert, C. Warsop, M. Forester and L. Axani, "DARPA CRANE – A toolset for the design of compact fluidic distribution systems for flow control applications: Part 2 – Model validation and implementation," in *AIAA SciTech Forum*, National Harbor, MD, 2023.

[28] R. P. Geraets, W. J. Crowther, M. K. Quinn, S. Weigert, T. Shearwood and M. R. A. Nabawy, "DARPA CRANE - Experimental investigation of the effectiveness of Coanda reaction surface geometries for Super-Critical Circulation-Control," in *AIAA SciTech Forum*, National Harbor, MD, 2023.

[29] 3M Closure Making and Systems Division, "Technical Data Sheet: 3M Scotch Transparent Film Tape 600," 11 November 2018. [Online]. Available: https://multimedia.3m.com/mws/media/2365814O/3m-scotch-transparent-film-tape-600.pdf?&fn=3M-Scotch-Transparent-Film-Tape-600.pdf. [Accessed 26 February 2024].

[30] R. W. Heidersbach, A. Pisano, A. Spens, V. A. Murnieks, D. Seth, M. H. McCrink and J. P. Bons, "Geometric Effects on the Aerodynamic Interactions of a Wing-Propeller Combination in Hover Flight," in *AIAA SciTech Forum*, Orlando, FL, 2024.

[31] ATI Industrial Automation, "F/T Sensor: Gamma," 2024. [Online]. Available: https://www.ati-ia.com/products/ft/ft_models.aspx?id=gamma. [Accessed 23 January 2024].

[32] M. G. Alexander, S. G. Anders, S. K. Johnson, J. P. Florance and D. F. Keller, "Trailing Edge Blowing on a Two-Dimensional Six-Percent Thick Elliptical Circulation Control Airfoil Up to Transonic Conditions," NASA Langley Research Center, Hampton, VA, 2005.

[33] R. T. Johnson, D. P. Witkowski and J. P. Sullivan, "Experimental Results of a Propeller/Wing Interaction Study," Society of Automotive Engineers, Inc., Wichita, Kansas, 1991.

[34] V. A. Murnieks, A. Spens, R. W. Heidersbach, D. Seth, M. H. McCrink and J. P. Bons, "Effectiveness of Various Trailing Edge Coanda Actuator Nozzles and Surfaces with a Propeller Slipstream Flow," in *AIAA SciTech Forum*, Orlando, FL, 2024.

[35] V. A. Murnieks, A. Spens, R. W. Heidersbach, D. Seth, M. H. McCrink and J. P. Bons, "Wing Trailing Edge Coanda Flow Control; Effect of Actuator Placement Relative to Upstream Propeller Slipstream," in *AIAA SciTech Forum*, Orlando, FL, 2024.

[36] G. J. Leishman, Principles of Helicopter Aerodynamics, 2nd ed., Cambridge University Press, 2016.

[37] R. Deters and G. K. S. M. K. Ananda, "Slipstream Measurements of Small-Scale Propellers at Low Reynolds Number," in *AIAA Applied Aerodynamics Conference*, Dallas, TX, 2015.

[38] D. P. Witkowski, A. K. H. Lee and J. P. Sullivan, "Aerodynamic Interaction Between Propellers and Wings," *J. AIRCRAFT*, vol. 26, no. 9, pp. 829-836, 1989.

Appendix A. Uniformity Data for Varying AFC Configuration Testing

Table A1: Exit slot velocity characteristics of CC-R8-H0.5 at multiple mass flow rates.

Mass Flow (g/s)	Minimum (m/s)	Maximum (m/s)	Average (m/s)	% Difference	Standard Deviation (m/s)
2	15.30	22.16	19.63	34.94	2.55
4	28.65	42.96	37.99	37.67	5.35
6	43.83	62.31	56.34	32.80	7.04
8	56.63	83.24	74.24	35.85	9.97

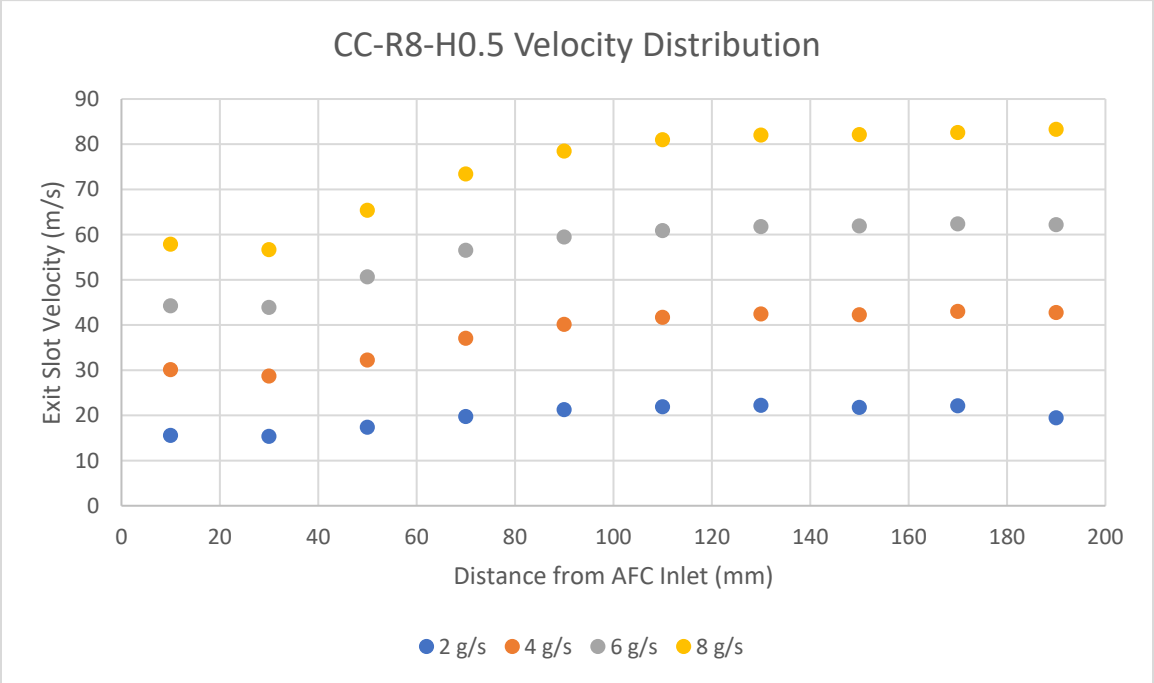

Figure A1: Exit slot velocity profiles of CC-R8-H0.5 at multiple mass flow rates.

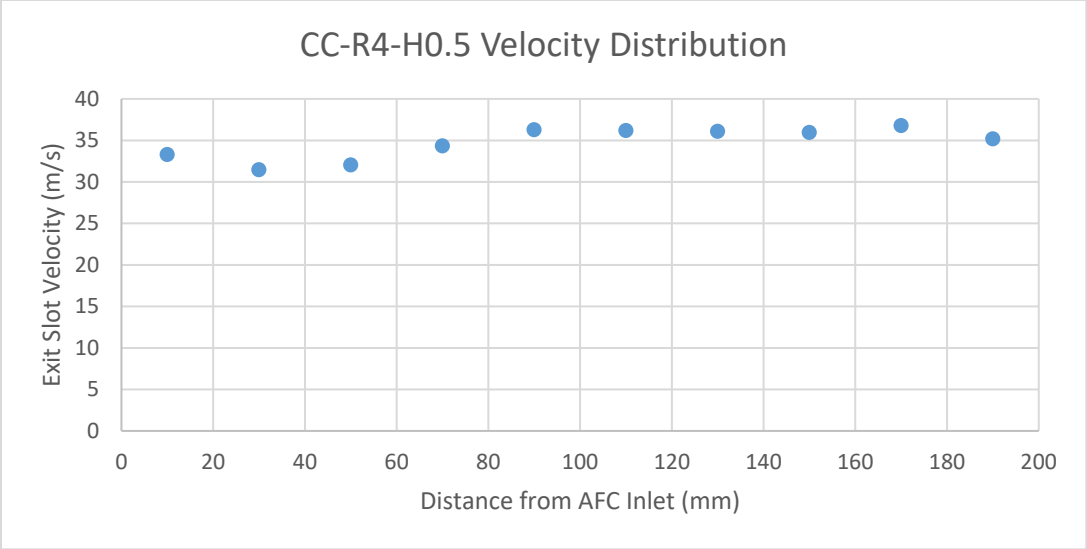

Figure A2: Exit slot velocity profiles of CC-R4-H0.5 at 4g/s.

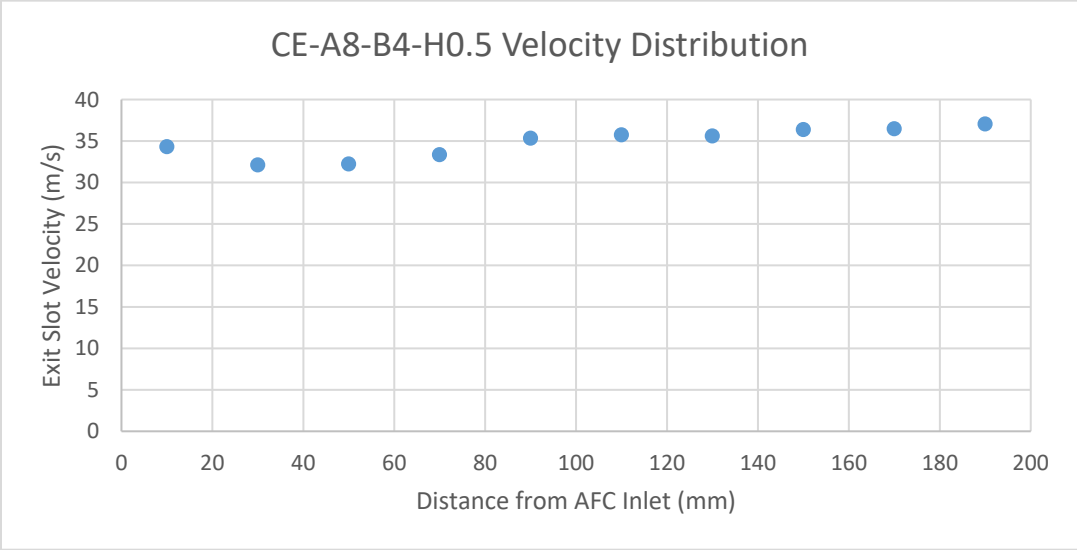

Figure A3: Exit slot velocity profile of CE-A8-B4-H0.5 at 4g/s.

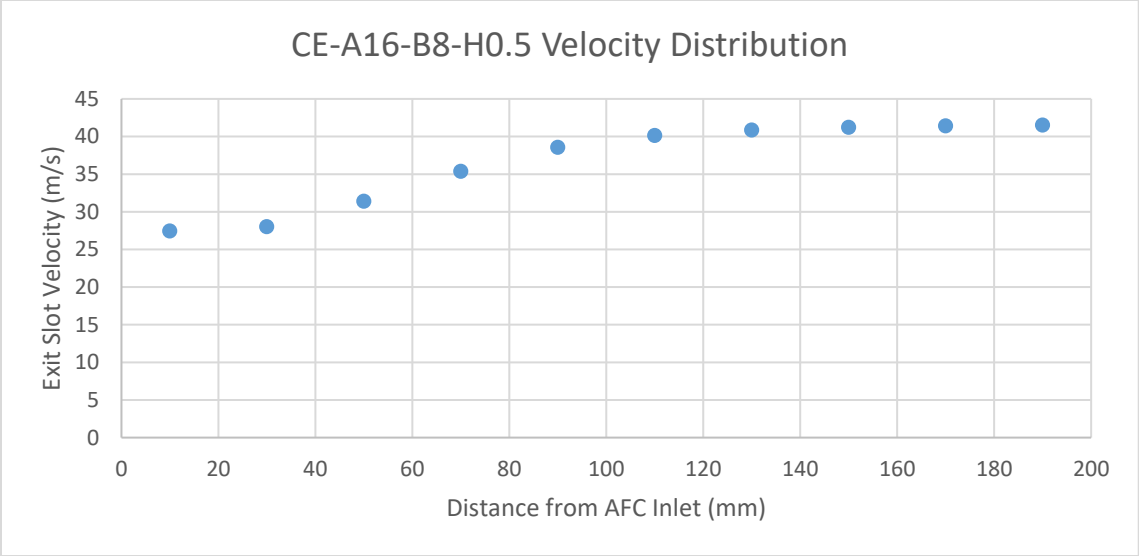

Figure A4: Exit slot velocity profile of CE-A16-B8-H1.0 at 4g/s.

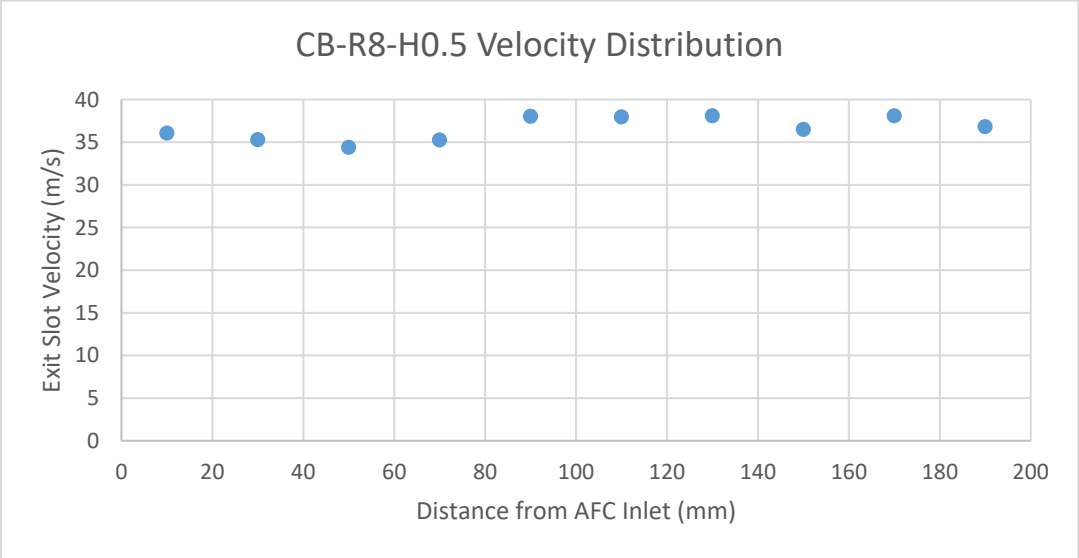

Figure A5: Exit slot velocity profile of CB-R8-H0.5 at 4g/s.

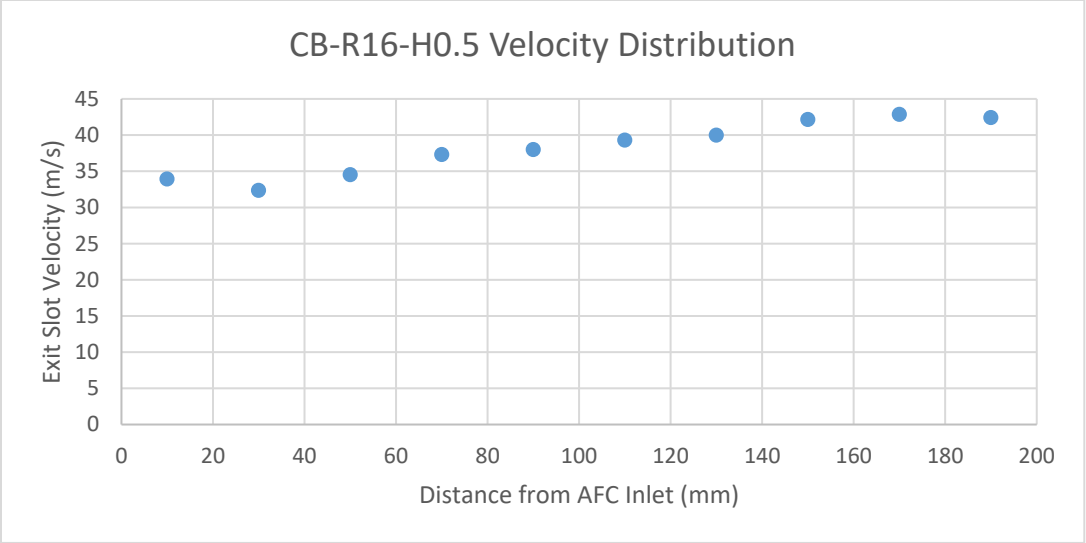

Figure A6: Exit slot velocity profile of CB-R16-H0.5 at 4g/s.

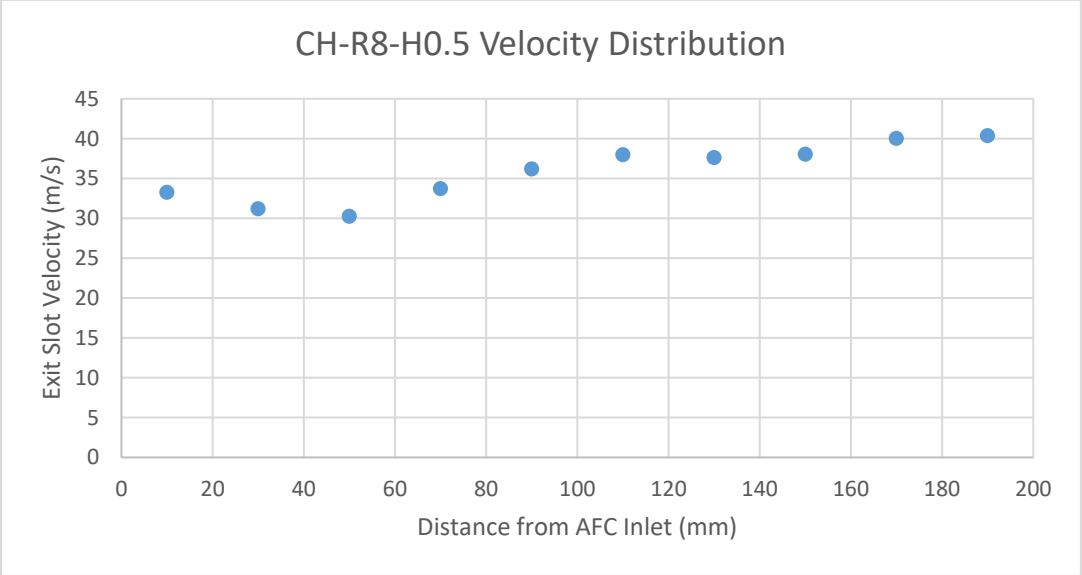

Figure A7: Exit slot velocity profile of CH-R8-H0.5 at 4g/s.

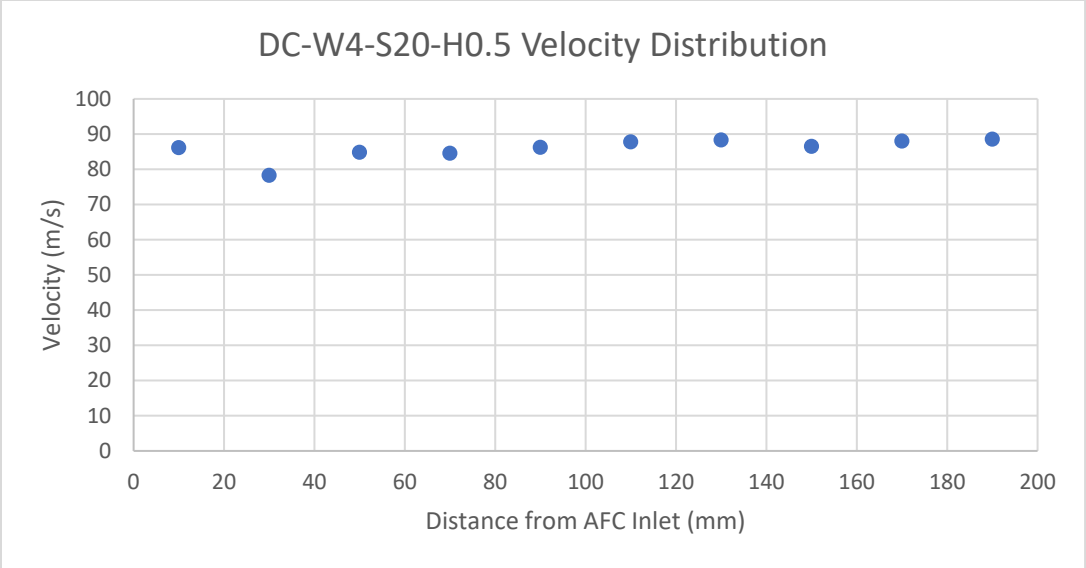

Figure A8: Exit slot velocity profile of DC-W4-S20-H0.5 at 2g/s.

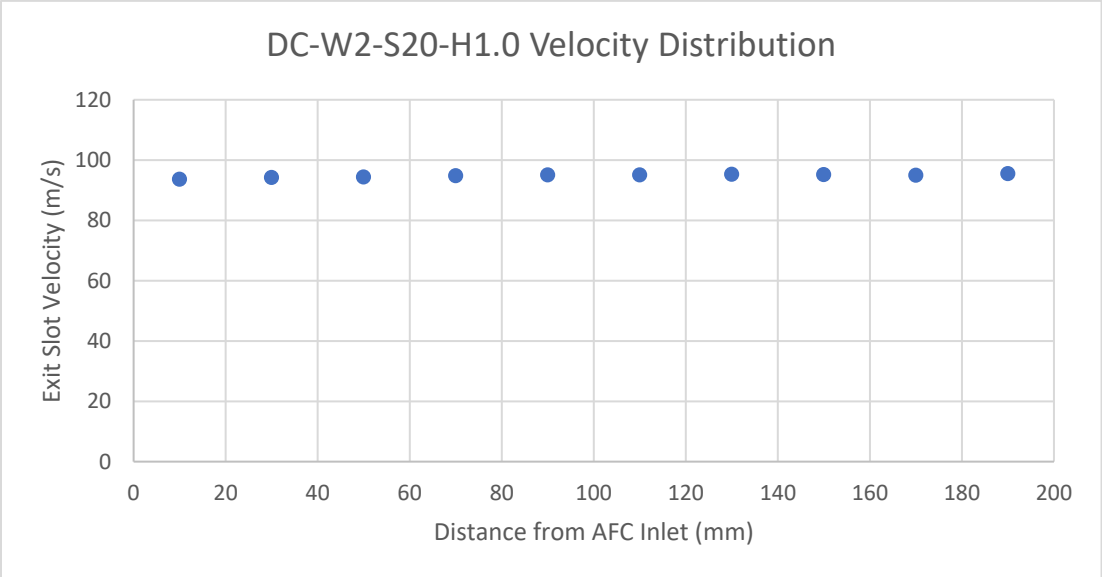

Figure A9: Exit slot velocity profile of DC-W2-S20-H1.0 at 2g/s.

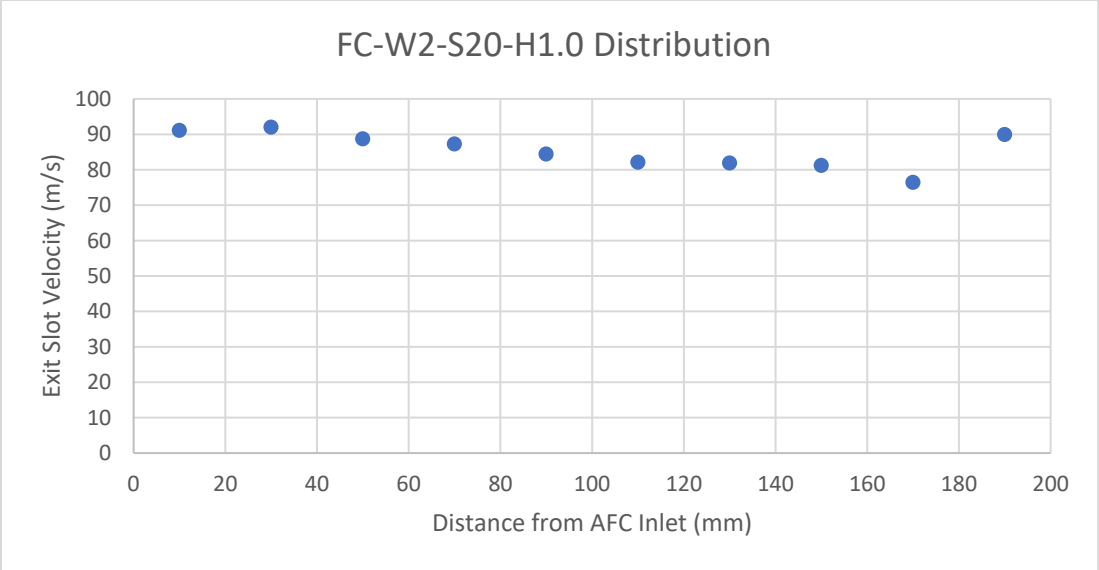

Figure A10: Exit slot velocity profile of FC-W2-S20-H1.0 at 2g/s.

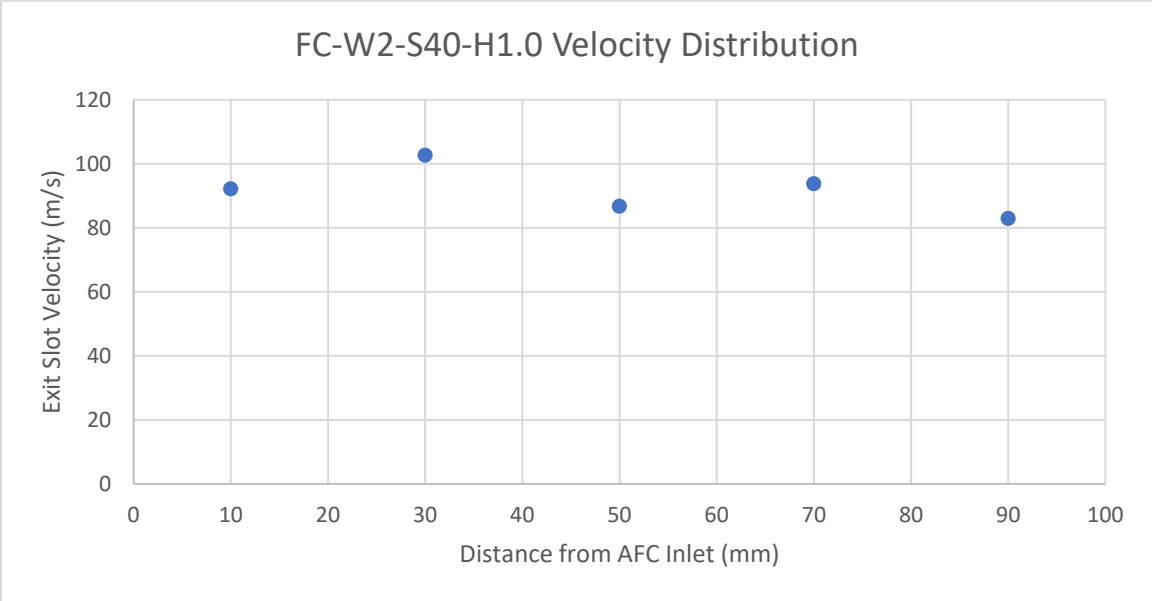

Figure A11: Exit slot velocity profile of FC-W2-S40-H1.0 at 1g/s.

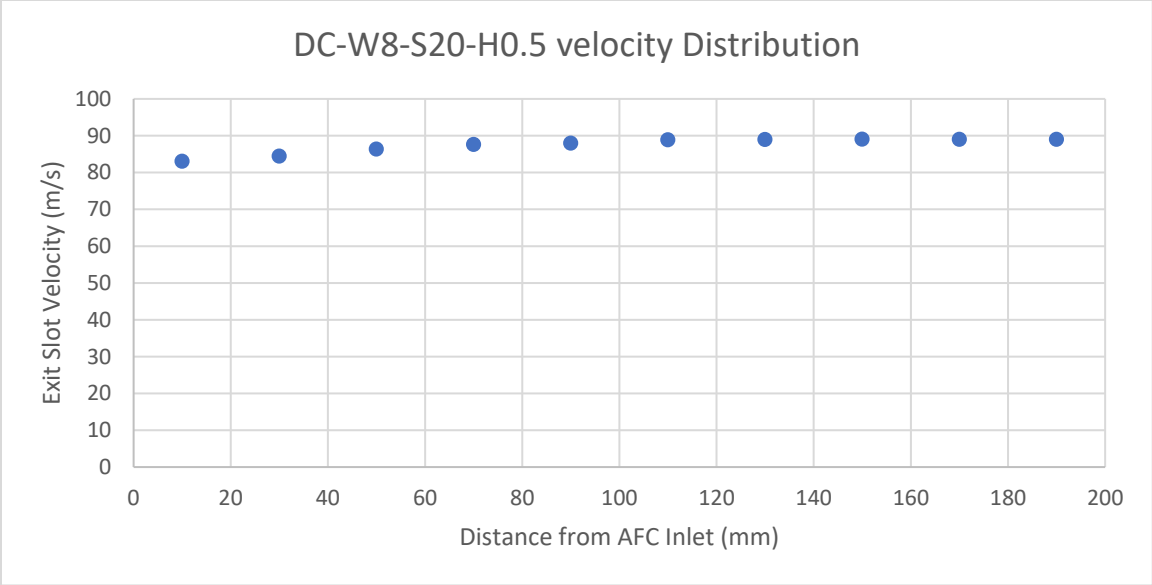

Figure A12: Exit slot velocity profile of DC-W8-S20-H0.5 at 4g/s.

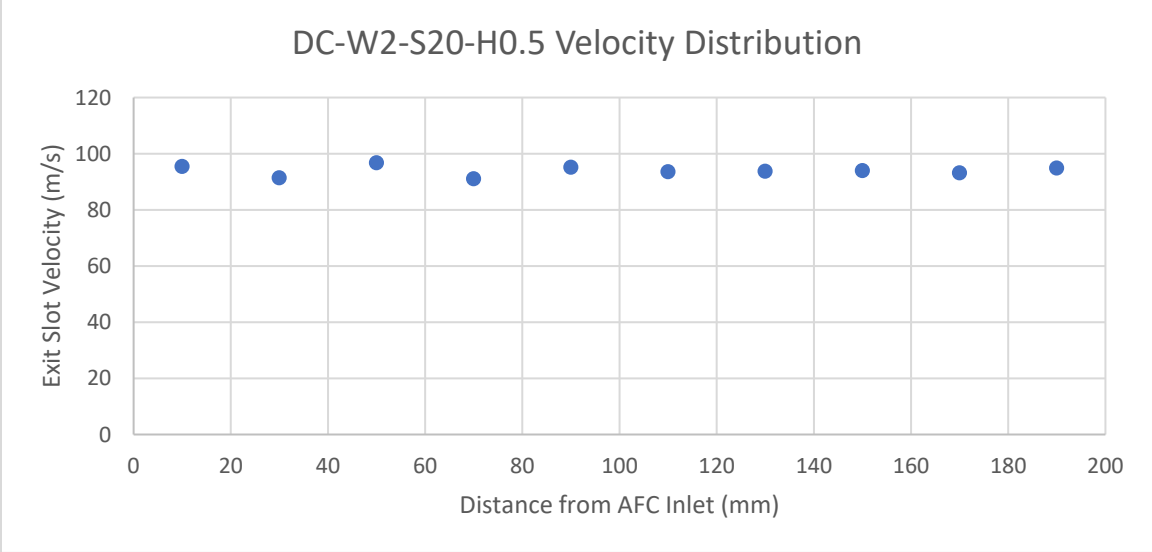

Figure A13: Exit slot velocity profile of DC-W2-S20-H0.5 at 1g/s.

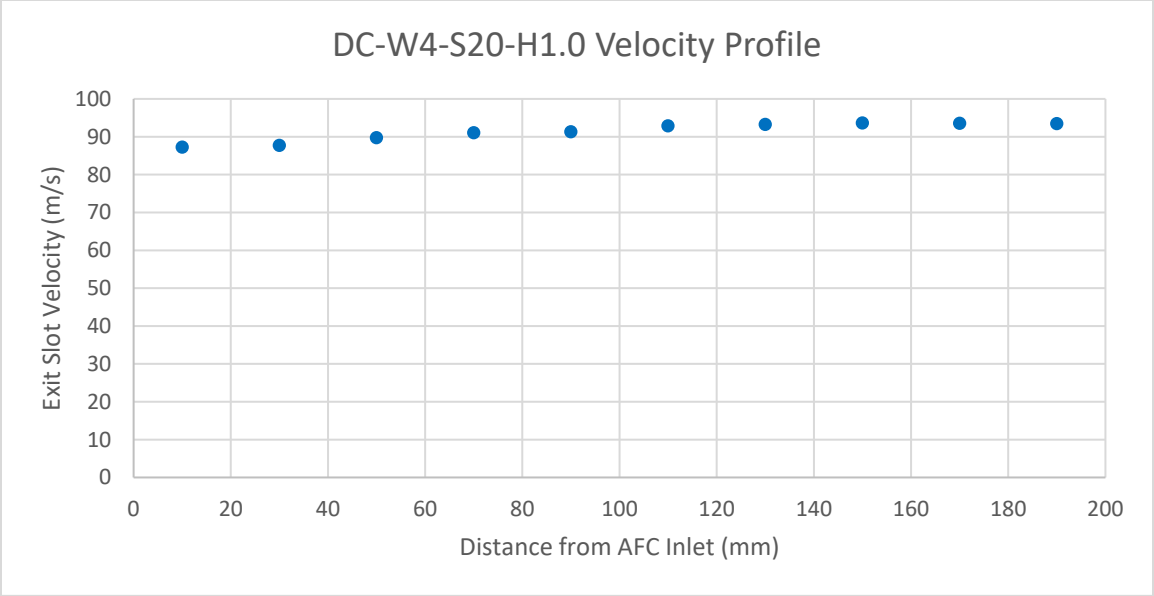

Figure A14: Exit slot velocity profile of DC-W4-S20-H1.0 at 4g/s.